Quantifying the spatial-seasonal patterns of land-atmosphere water, heat and CO_2 flux exchange over the Tibetan Plateau from an observational perspective

Binbin Wang[1,2,5,6,7], Yaoming Ma[1,2,3,4,5,6,7*], Zeyong Hu[8], Xuan Li[1], Weiqiang Ma[1,2,4,5,6,7], Xuelong Chen[1,2,5,6,7], Cunbo Han[1,2,5,6,7], Zhipeng Xie[1,2,5,6,7], Yuyang Wang[9], Maoshan Li[10], Bin Ma[1,5,6,7], Xingdong Shi[1,4,7], Weimo Li[1,4], Zhengling Cai[1,4]

[1]State Key Laboratory of Tibetan Plateau Earth System, Resources and Environment (TPESRE), Institute of Tibetan Plateau Research, Chinese Academy of Sciences, Beijing 100101, China;

[2]College of Earth and Planetary Sciences, University of Chinese Academy of Sciences, Beijing 100049, China;

[3]College of Hydraulic & Environmental Engineering, China Three Gorges University, Yichang 443002, China;

[4]College of Atmospheric Science, Lanzhou University, Lanzhou 730000, China;

[5]National Observation and Research Station for Qomolongma Special Atmospheric Processes and Environmental Changes, Dingri 858200, China;

[6]Kathmandu Center of Research and Education, Chinese Academy of Sciences, Beijing 100101, China;

[7]China-Pakistan Joint Research Center on Earth Sciences, Chinese Academy of Sciences, Islamabad 45320, Pakistan;

[8]Key Laboratory of Land Surface Process and Climate Change in Cold and Arid Regions, Northwest Institute of Eco-Environment and Resources, Chinese Academy of Sciences, Lanzhou, 730000, China;

[9]College of Grassland Science and Technology, China Agricultural University, Beijing, 100193,China;

[10]School of Atmospheric Sciences, Chengdu University of Information Technology, Chengdu 610225, China

Corresponding authors: Binbin Wang (wangbinbin@@itpcas.ac.cn); Yaoming Ma (ymma@itpcas.ac.cn); Address: Building 3, Courtyard 16, Liucui Road, Chaoyang District, Beijing City, China. Zip code: 100101.

Abstract

Land-atmosphere (LA) interactions, through the turbulent exchange of water, heat and CO_2 fluxes, strongly influence regional micro-climates, water cycles, energy budgets, and ecosystem dynamics. The Tibetan Plateau (TP), characterized by its vast extent, high elevation, strong solar radiation and extreme weather variability, remains underexplored due to the scarcity of LA observation sites, particularly in its western and northern regions. This study introduces a newly established research and observation platform, comprising 16 planetary boundary layer towers that span diverse landscapes and dynamic meteorological conditions. Across these sites, mean annual air temperature, wind speed, and liquid precipitation range from -3.5 to 18.5°C, 0.6 to 5.6 m s^{-1}, and 43 to 2164 mm, respectively. Elevation exhibits significant correlations with all meteorological variables, highlighting the pronounced spatial heterogeneity of land–atmosphere coupling across the region. The turbulent fluxes of water and heat exhibit distinct seasonal patterns, with maximum sensible heat flux (*SH*) in April-May and latent heat flux (*LE*) in July-August. Most stations act as carbon sinks, with net ecosystem exchange (*NEE*; the net CO_2 exchange between the ecosystem and the atmosphere, where negative values indicate net ecosystem CO_2 uptake) ranging from -3.2 to -174.3 g C m^{-2} a^{-1}, except the Medog station, which behaves as a carbon source likely linked to vegetation disturbance and human activity. *LE* is significantly correlated with *SH*, *NEE* and ecosystem respiration, revealing a strong coupling among water, heat and carbon fluxes. This high-resolution, quality-controlled dataset provides critical in situ observations for studying water–heat–carbon coupling, validating models and satellite algorithms, and improving understanding of climate-ecosystem interactions over the TP. The whole datasets are freely available at the National Tibetan Plateau Data Center (https://doi.org/10.11888/Atmos.tpdc.302428).

Key words: Land-atmosphere turbulent fluxes, spatial-temporal variations, comprehensive observation and research platform, Tibetan Plateau

1 Introduction

Land-atmosphere (LA) interactions, which govern the flux exchanges of energy, water, and CO_2 between the Earth's surface and the atmosphere, are pivotal in shaping regional water cycles, climate dynamics, and ecosystem changes [*Gentine et al., 2019; Ma et al., 2023; Santanello et al., 2018; Seo and Ha, 2022; Zhang et al., 2024*]. Thermal contrasts between distinct landforms—such as land vs. water, mountain vs. valley, and ocean vs. land — drive regional circulations like lake-land and mountain-valley breezes, as well as large-scale atmospheric motions, including monsoons [*Gerken et al., 2014; Wu and Zhang, 1998; Wu et al., 2023*]. These LA interactions modulate a wide range of processes, including the dispersion of air pollutants, the transport of atmospheric moisture, the redistribution of clouds and precipitation, and the regulation of ecosystem carbon balance [*Bei et al., 2018; Friedlingstein et al., 2022; Suni et al., 2015; Zhu et al., 2017*]. For instance, enhanced coupling between soil moisture and land surface temperature can intensify droughts and heatwaves in northern East Asia [*Seo and Ha, 2022*], where soil moisture deficits reduce evapotranspiration (*ET*), amplifying heatwave conditions, particularly in areas with sparse vegetation. Nonlinear feedbacks between *ET* and cloud formation remain poorly constrained in transitional zones between energy- and water-limited regimes [*Zhang et al. 2024*]. Under global warming, LA interactions governing permafrost thaw, vegetation productivity, and ecosystem respiration play an increasingly important role in determining regional and global carbon budgets, especially over the data scarce regions [*Turetsky et al., 2020; Wang et al., 2023b; Wei et al., 2021*]. Quantifying these coupled fluxes through in situ observations is thus essential for understanding Earth system responses to climate change.

Understanding LA interactions through coordinated, multidisciplinary, and multi-scale observations is crucial for addressing global challenges such as water resource management, land-use planning, climate change, and ecosystem preservation. In this context, key global initiatives—such as the First International Satellite Land Surface Climatology Project Field Experiment (United States) [*Sellers et al., 1992*], the Hydrologic Atmospheric Pilot Experiment (France, Niger) [*André et al., 1986; Goutorbe et al., 1997*], the Northern Hemisphere Climate Processes Land Surface Experiment (Sweden) [*Halldin et al., 1999*], the Boreal Ecosystem–Atmosphere Study (Canada) *[Sellers et al., 1995]*, the Inner Mongolia Semiarid Grassland Soil–Vegetation–Atmosphere Interaction and the Heihe River Basin Field Experiment (China) [*Liu et al., 2018; Lü et al., 1997*]—have provided foundational insights into LA interactions and have advanced parameterizations for climate models. Tibetan Plateau (TP), one of the world's most climate-sensitive and data-scarce region, plays a particularly critical role in the climate and ecology dynamics. TP exerts remarkable influence on atmospheric processes, generating thermal disturbances that affect circulation patterns, weather, and climate not only in China and East Asia but also globally[*Wu and Zhang, 1998; Ye and Wu, 1998*]. For example, mesoscale system vortices and shear lines created in the TP's atmospheric boundary layer can lead to extreme weather events, such as heavy rain and storms, impacting both the plateau and surrounding regions [*Li et al., 2020; Xu and Chen, 2006*]. Thus, LA coupling and dynamics are important for the formation and development of weather systems. Over the past few decades, large-scale field activities and long-term observational experiments—such as Qinghai-Xizang Plateau Meteorology Experiment (QXPMEX), the Tibetan Plateau Atmospheric Scientific Experiment II and III (TIPEX-II, TIPEX-III), the Sino Japanese inter governmental cooperation project (JICA), the Global Energy and Water Cycle Experiment Asian Monsoon Experiment on the Tibetan Plateau (GAME/Tibet), the Coordinated Enhanced Observing Period (CEOP) Asia-Australia Monsoon Project on the Tibetan Plateau (CAMP/Tibet), etc. —have greatly enhanced our understanding

of land surface processes in the TP *[Huang et al., 2023; Ma et al., 2023]*, and these efforts have also helped refine climate model parameterization, improving our ability to predict TP's climatic effects. However, the stations for measuring heat, water and CO_2 fluxes are concentrated mostly in the east and still rarely distributed over the vast northern and western regions, hindering our understanding on its spatial distribution and total amounts of heat, water and CO_2 flux. Given the growing challenges posed by global climate change, accurately measuring and modeling LA interaction processes is more critical than ever, and such efforts are essential for predicting climate extremes, managing water resources, and supporting sustainable ecology [*Suni et al., 2015*].

Although several LA interaction studies have analyzed seasonal variations in turbulent fluxes and their controlling factors [Ma et al., 2005; Ma et al., 2018; Ma et al., 2023; Wang et al., 2011; Yang et al., 2008], the lack of spatially distributed eddy-covariance (EC) sites has resulted in large uncertainties in flux estimates and interannual variability, especially over underrepresented ecosystem types over the western and northern TP. Previous modeling and remote-sensing efforts have improved regional *ET* estimates, yet still rely on limited ground validation measurements [*Ma and Zhang, 2022; Yuan et al., 2024*]. For example, the water-carbon coupled biophysical model [*Ma and Zhang, 2022*] and an improved *ET* model *[Yuan et al., 2021]* are validated with EC measurements, both yielding annual *ET* value of approximately 350 mm yr^{-1}. However, factors influencing the inter-annual variations in *ET* exhibit large biases and uncertainties, especially for data-scarce western and northern regions. As for carbon function, TP contains extensive permafrost and a variety of landscapes, including alpine meadows, alpine steppes, alpine shrubs, alpine wetlands, forests, and alpine deserts, which have a substantial impact on the carbon sink/source function of the region, and shows important ecological and environmental consequences. Recent studies indicate that most alpine meadows on the TP function as carbon sinks, with values ranging from -430 to -12.5 g C m^{-2} a^{-1}, and some alpine steppe areas act as weak carbon sources [*Wang et al., 2023a; Wei et al., 2021*]. Specifically, alpine grasslands exhibit a weaker carbon sink function, with values ranging from -206.9 to -17.1 g C m^{-2} a^{-1} whilst shrub lands show even lower carbon sink values, ranging from -89.5 to -40.7 g C m^{-2} a^{-1} [*Wei et al., 2021*]. Marshes display considerable variability in carbon fluxes, with values ranging from -187 ± 29 g C m^{-2} a^{-1} in Shenzha to -478 g C m^{-2} a^{-1} in Haibei [*Qi et al., 2021; Zhao et al., 2005*]. Therefore, by synthesizing EC and climate data from multiple sites across the TP, we can clearly understand the spatial and temporal variations of water, heat, CO_2 fluxes and identify the mechanisms that control them.

To address these knowledge gaps, this study introduces a comprehensive multi-site observation network for monitoring LA exchanges of water, heat, and CO_2 fluxes across the TP (Figure 1 and Table 1). The dataset encompasses 16 stations strategically distributed along major hydrothermal and ecological gradients, including alpine meadow, steppe, shrubland, and forest ecosystems. These standardized, long-term EC observations provide unprecedented spatial coverage, particularly over the data-scarce western and northern TP. The network offers a unique opportunity to investigate (1) What are the characteristics of land-atmosphere water, heat, and CO_2 fluxes across different landscapes of the TP? (2) What are the spatial and temporal distributions of water, heat, and CO_2 fluxes, and what factors influence these variations? This paper introduces the design and implementation of the observation platform, instrument configuration, and standardized data processing methods, followed by an analysis of the spatial–temporal variations of meteorological conditions, energy components, and CO_2 fluxes. Spefically, section 3.1 describes the spatial–temporal patterns of atmospheric meteorological variables such as air temperature, humidity and wind speed. Section 3.2 focuses on liquid precipitation and soil

water content, which jointly reflect regional water availability. Section 3.3 examines the energy flux components (sensible and latent heat fluxes, etc.), highlighting differences between wet and dry conditions and section 3.4 analyzes the seasonal variations of carbon fluxes (net ecosystem exchange (*NEE*), gross primary productivity (*GPP*) and ecosystem respiration (*Re*)). By making this dataset publicly available, we aim to fill a critical gap in global flux observations and provide a foundation for advancing land–atmosphere interaction research, model evaluation, and climate prediction over high-elevation ecosystems of the TP.

# 2 The observation platform and methods

2.1 Introduction of observation platform and instruments configuration

Long-term and quasi-continuous EC networks have been established worldwide across diverse ecosystems, including AmeriFlux and Fluxnet-Canada in North America, EuroFlux and CarboEurope in Europe, AsiaFlux and ChinaFlux in Asia, and OzFlux in Australia [Baldocchi, 2014; Yu et al., 2024]. These networks provide critical ground-based measurements for understanding LA energy and material exchanges. Given the TP's vast area (approximately 2.6 million km^2) and extreme environmental conditions — such as high solar radiation, large diurnal temperature variations, and limited precipitation—such EC observations are especially valuable. In this context, the Institute of Tibetan Plateau Research, Chinese Academy of Sciences, established six comprehensive and long-term LA interaction stations in remote and data-scarce regions of TP gradually since 2004 [*Ma et al., 2008*], including QOMOS (the Qomolangma Atmospheric and Environmental Observation and Research Station, CAS), NAMORS (the Nam Co Monitoring and Research Station for Multisphere Interactions, CAS), SETORS (the Southeast Tibet Observation and Research Station for the Alpine Environment, CAS), NADORS (the Ngari Desert Observation and Research Station, CAS), MAWORS (the Muztagh Ata Westerly Observation and Research Station, CAS), and Shuanghu. Since 2019, the 6 stations were upgraded with new sonic anemometer and gas analyzer sensors gradually (CSAT3 and LI7500DS), enhancing the measurement capabilities. The instrumentation and long-term data at 5 stations covering 2006–2021 can be found in Ma et al. [*2020*] and Ma et al. [*2024*].

Furthermore, the Second Tibetan Plateau Expedition and Research Program (STEP) in 2019 has expanded the network, adding 10 additional LA interaction stations, including Medog, Qamdo, Mangkam, Mangai, Baingoin, Nyima, Jyirong, Burang, Coqen, Lhasa, especially in the remote western and northern regions. The integrated EC devices (IRGASON, Campbell; CSAT3 & LI7500RS in Lhasa), capable of measuring high-frequency (10 Hz) quantities of sonic temperature, water, CO_2, and three-dimensional winds, have been used. This expansion resulted in the creation of the Third Pole Environment Integrated Three-dimensional Observation and Research Platform (TPEITORP, observation platform for short hereafter) for measuring water, heat, and CO_2 fluxes over the TP [*Ma et al., 2023*]. All stations are equipped with 20 m planetary boundary layer (PBL) towers (40 m at Lhasa) that continuously measure a comprehensive set of meteorological and flux variables. These include air pressure, liquid precipitation, infrared land surface temperature, four-component radiation, soil temperature and moisture at multiple depths, air temperature and humidity at five vertical levels, wind speed and direction at five levels, as well as turbulent fluxes of water, heat, and CO_2. Turbulent fluxes were measured using an EC system installed on each tower, with sensor height and orientation optimized according to prevailing wind directions and local surface roughness conditions. The details of the instrument configuration, station locations, and photographs are provided in Table 1 and Figure 1, respectively. In-situ measurements from

205   these stations, with updated systems, were utilized to analyze the seasonal and diurnal variations of water,
206   heat, and CO_2 fluxes, as well as the associated energy budget and carbon source–sink dynamics across
207   contrasting ecosystems and climates. A detailed illustration of the observational environments at 16
208   stations are as follows.
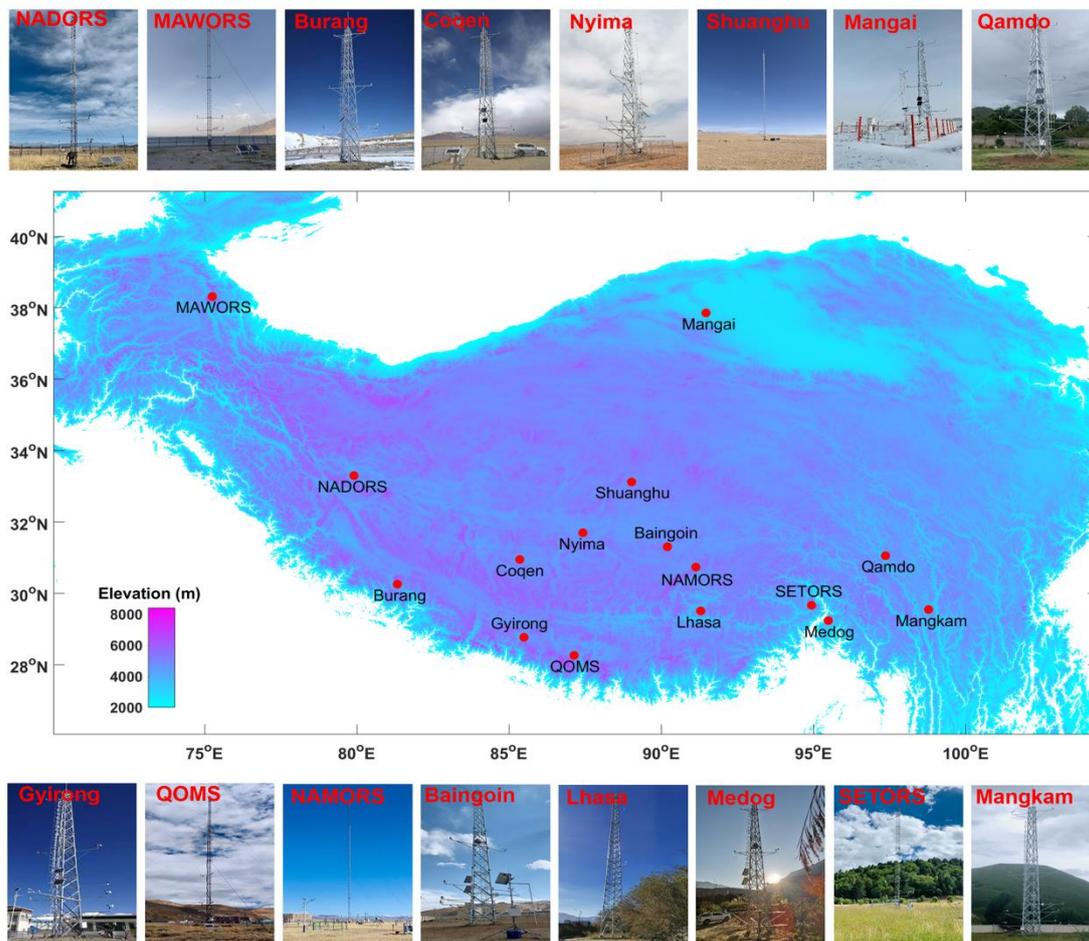
209
210   **Figure 1.** The locations and photos of 16 LA interaction stations composing the comprehensive
211   observation and research platform over the TP. (All the photos have been taken by the authors)

212   QOMOS station is located in Rongbuk Valley, north of Mt. Everest, with a flat observation field
213   dominated by barren land and sparse vegetation. NAMORS station, on the southeast bank of the third
214   largest lake (Nam Co) in TP, is covered by alpine meadow. Both QOMOS and NAMORS have in situ
215   EC and PBL tower systems that have been in operation since 2005, with sensors upgraded in 2019.
216   SETORS station, located in a mountain valley in the southeast TP, is covered with dense vegetation (50–
217   60 cm high). The EC and PBL systems were first installed in 2007 and fully upgraded in 2020. NADORS
218   station, in grassland near Ritu County and Bangong Co, has had an EC system and an automatic weather
219   station (AWS) since 2008, with a new 20 m PBL tower and a new EC system installed in 2020. MAWORS
220   station, located near Mustag Mountain and Karakori Lake in Xinjiang, is influenced by westerly winds.
221   The station has been equipped with an EC system since 2010, and both EC and PBL systems were
222   updated in October 2020. Shuanghu station, located 3 km north of Shuanghu County, has been
223   operational since 2012, with a typical alpine grassland surface. The original EC system is still in use,
224   with new EC and PBL systems added in 2021.

Table 1. Overview of instruments configuration and settings at 16 stations, including observation variables, instrument sensors, observational heights, latitude (lat), longitude (lon), altitude (alt) and landscape at each station.

Variables	Sensors (Manufacturers)	Heights	Stations (lat, lon, alt, landscape)
Air temperature and humidity	HMP155A-L (Vaisala)	1.5, 2, 4, 10, and 20 m	1. QOMOS (28.36ºN, 86.95ºE, 4276 m, Alpine desert); 2. NAMORS (30.77ºN, 90.98ºE, 4730 m, Alpine steppe); 3. SETORS (29.77ºN, 94.73ºE, 3327 m, Alpine meadow); 4. NADORS (33.39ºN, 79.7ºE, 4270 m, Alpine desert); 5. MAWORS (38.41ºN, 75.05ºE, 3668 m, Alpine desert); 6. Shuanghu (33.22ºN, 88.83ºE, 4947 m, Alpine steppe); 7. Lhasa (40.01 ºN, 116.38 ºE, 3650 m, City)
Wind speed and direction	05103-L (R.M.Young)	1.5, 2, 4, 10, and 20 m	
Air pressure	CS106 (Vaisala)	-	
Radiations	CNR4 (Kipp & Zonen)	1.5 m	
Precipitation	RG3 (Onset)	-	
Soil temperature and moisture	CS655 (Campbell)	0.1, 0.2, 0.4, 0.8 and 1.6 m	
Soil heat flux	HFP01 (Hukseflux)	0.1 and 0.2 m	
Turbulent flux	CSAT3B (Campbell)；LI-7500DS (Li-COR)	Site specific	
Air temperature and humidity	HMP155A (Vaisala)	1, 2, 4, 10 and 20 m	8. Medog (29.32ºN, 95.29ºE, 820 m, Forest); 9. Qamdo (31.15ºN, 97.17ºE, 3307 m, Alpine steppe); 10. Mangkam (29.64ºN, 98.59ºE, 3840 m, Alpine meadow); 11. Mangai (37.95ºN, 91.7ºE, 3073 m, Bare ground); 12. Baingoin (31.4ºN, 90.01ºE, 4709 m, Bare ground); 13. Nyima (31.79ºN, 87.23 ºE, 4573 m, Alpine steppe); 14. Jyirong (28.86 ºN, 85.29 ºE, 4140 m, Bare ground); 15. Burang (30.35 ºN, 81.14 ºE, 4113 m, Bare ground); 16. Coqen (31.04 ºN, 85.16 ºE, 4683 m, Alpine steppe);
Wind speed and direction	05103 (R.M.Young)	1, 2, 4, 10 and 20 m	
Air pressure	PTB110 (Vaisala)	-	
Radiations	CNR4 (Kipp & Zonen)	1.5 m	
Precipitation	RG3 (Onset)	-	
Soil temperature and moisture	CS655 (Campbell)	0.1, 0.2, 0.4, 0.8, 1.6 m	
Soil heat flux	HFP01 (Hukseflux)	0.1 and 0.4 m	
Turbulent flux	IRGASON (Campbell)	Site specific	
Notes: the heights of turbulent flux measurements from station number 1 to number 16 are 3.0 m, 3.77 m, 3.13 m, 3.7 m, 3 m, 3.2 m, 5 m, 5.5 m, 5.5 m, 3.5 m, 3.5 m, 5.5 m, 3.8 m, 3.5 m, 3.5 m and 40 m respectively. In Lhasa station, the heights of atmosphere variables at 5 layers are 2 m, 4 m, 8 m, 16 m, 32 m.			

The stations of Medog, Qamdo, Mangkam, Mangai, Baingoin, Nyima, Jyirong, Burang, Coqen and Lhasa were gradually established till 2021 with support from STEP program. Medog, Qamdo, and Mangkam stations are located in the southeastern TP. Medog is located at the southern foot of the eastern Himalayas, near the Yarlung Zangbo River, with a steep terrain surrounded by subtropical evergreen broadleaf forest (i.e. banana trees) and crops (i.e., peanuts). Qamdo is situated in the Changdu Meteorological Bureau's observation field, covered by grass at the top of hilly Changdu City. Mangkam

234 is located at the Mangkang County Meteorological Bureau's external observation field, with a surface
235 covered by 10 cm grass. Mangai station is in the northern part of the TP, with a Gobi desert landscape.
236 The PBL tower and EC system were mounted on the Mangai Meteorological Bureau's external
237 observation field. Baingoin, Nyima, and Coqen stations are located in the west-central TP, each with PBL
238 and EC systems installed at their respective County Meteorological Bureau's observation fields. The land
239 surfaces are bare ground, alpine meadow and alpine meadow, respectively. Jyirong and Burang, located
240 north of the Himalayas, are covered by sparse vegetation and bare land, respectively. Lhasa station,
241 constructed in 2020 and having a 40 m PBL tower, is located in the field observation base of ITPCAS,
242 with roads and low-level buildings surrounded.

243 These stations are distributed across various climatic and environmental regions, covering
244 landscapes such as alpine desert, alpine steppe, alpine meadow, bare ground and city. Some stations,
245 including Mangkam, Baingoin, Qamdo and Lhasa are situated in or adjacent to cities, thus they can be
246 influenced by nearby human activities to some extent. The land surface properties (e.g., land cover,
247 terrain, soil texture) and local climate vary markedly across stations, providing valuable data for
248 generalizing LA interaction schemes across diverse environments and climates over the TP. These
249 differences highlight the complexity of coupled LA interactions, the challenges in obtaining necessary
250 data for model development, and the need for a comprehensive understanding of how land surface
251 processes affect atmospheric conditions and climate predictability. After the construction of the
252 observation platform in 2021, the instruments calibration and maintenance have been carried out twice a
253 year, with field work distance of more than 5000 km and duration of more than 1 month each time. Our
254 efforts to maintain this observation platform aim to bridge the observational gaps in data-scarce regions
255 and to support research on land surface processes, water and energy cycles, and environmental effects
256 across the TP.

2.2 Methods for data processing and analyzing

258 To study the spatial-temporal variations of meteorological variables and turbulent fluxes of water,
259 heat and CO_2 at these stations and to analyze the influencing factors over the different climatic and
260 environmental conditions, 15 stations have been chosen in this study with an exception of Lhasa, which
261 only captured the measurements during the daytime because of the power malfunction at night. We
262 selected field measurements of more than 2 years, mostly covering the period of May 2021 to July 2023.
263 The proportions of data coverage for meteorological variables and turbulent flux are close to 94% and
264 77%, respectively, with the least data integrity percentage of approximately 50% in Mangai station.
265 Details of data coverage at each station can be found in Table S1 in supplementary material. After
266 accounting for data losses due to instrument failure, power interruptions, and occasional human
267 operational errors, precipitation records from July 2021 to June 2022 were used in this study.
268 Precipitation data gaps occurred at three stations—QOMS (20 %, Feb 1 – Feb 14, May 14 – Jun 1, 2022),
269 NAMORS (22 %, Jan 1 – Mar 21, 2022), and SETORS (6 %, Feb 8 – Feb 12, Mar 27 – Apr 12, 2022)—
270 with the missing periods distributed intermittently throughout the observation year. These data gaps were
271 primarily caused by technical or operational issues. As the rain gauge (RG3, Onset) measures only liquid
272 precipitation during warm seasons and does not record solid precipitation in cold months, the missing
273 data, mostly during winter and pre-monsoon periods, do not affect the conclusions regarding the spatial
274 and temporal variations of liquid precipitation.

275   Currently, meteorological variables were processed following standardized protocols. Abnormal
276   values—defined as physically implausible measurements such as downward shortwave radiation greater
277   than 1360 W m^{-2} or less than 0 W m^{-2}, or variables showing unrealistic diurnal or seasonal patterns caused
278   by sensor or power malfunctions—were flagged and removed after visual inspection and consistency
279   checks. For turbulent heat flux, two types of open-path EC systems were used across the stations:
280   CSAT3B and LI-7500DS (stations 1–7) and IRGASON (stations 8–16). These high frequency data were
281   processed using standard EddyPro software, which includes standard procedures of spike removal,
282   buoyancy flux conversion to sensible heat, double rotation, as well as ultrasonic virtual temperature
283   correction and density correction (Webb-Pearman-Leuning correction) [*Massman and Lee, 2002;*
284   *Mauder and Foken, 2006; Twine et al., 2000*]. Quality flags are applied to the flux estimates, considering
285   steady state test and integral turbulence characteristics test [*Mauder et al., 2013*]. *NEE* represents the net
286   vertical CO$_2$ flux between the ecosystem and the atmosphere and is directly measured by the EC system.
287   The two main components of the carbon cycle, *GPP* and *Re*, are then estimated from the measured *NEE*
288   using the standard flux partitioning procedures implemented in the REddyProc package [*Wutzler et al.,*
289   *2018*], where a temperature response function for *NEE* fluxes is used to represent *Re*, with *GPP* derived
290   as the difference between *Re* and *NEE*. Nighttime *NEE* data with low friction velocity were filtered to
291   avoid biases, and gaps were filled using the available meteorological data. Specifically, the friction
292   velocity threshold was estimated using the bootstrapping approach implemented in REddyProc,
293   following the standard procedure described by Wutzler et al. [2018]. Flux gap-filling was performed
294   using the marginal distribution sampling method within REddyProc, which estimates missing values
295   based on relationships with radiation, air temperature, and vapor pressure deficit within a 7-14 day
296   moving window. Quality control procedures included removing data points affected by sensor
297   malfunction, spikes, or physically implausible fluxes, and applying the flagging schemes of Mauder et
298   al. (2013). All low-quality or filtered data were excluded prior to gap-filling and flux partitioning to
299   ensure data integrity.

300   Diurnal and seasonal variations of meteorological and turbulent flux variables were analyzed after
301   filtering out low-quality and spurious data. To reduce the influence of data gaps and enhance
302   comparability among sites, monthly averaged diurnal cycles of meteorological variables and turbulent
303   fluxes were used to examine their spatial and temporal patterns across stations. The total annual values
304   for *ET*, *NEE*, *GPP* and *Re* were obtained by summing the monthly values. During data quality screening,
305   three stations (QOMOS, NAMORS, and Baingoin) were excluded from the *NEE* flux synthesis because
306   their *NEE* diurnal cycles exhibited physically inconsistent behavior. Specifically, QOMOS and
307   NAMORS showed inverted daytime-nighttime variations, while Baingoin displayed abnormally
308   nighttime CO$_2$ emissions, probably influenced by nearby biomass burning. Only the remaining 12
309   stations with reliable CO$_2$ flux data were retained for spatial and temporal analyses. The energy budget
310   ratio (*EBR*) and Bowen ratio (*Bo*) at each station were estimated to evaluate energy conditions and energy

311   consumption. *EBR* ($EBR = \frac{\sum LE+SH}{\sum R_n - G}$) compares the cumulative sum of available energy inputs to the

312   cumulative sum of turbulent energy outputs over an entire year. Available energy inputs include net
313   radiation (R_n, W m^{-2}) and ground heat flux (G, W m^{-2}) while turbulent energy outputs include latent heat
314   flux (*LE*, W m^{-2}) and sensible heat flux (*SH,* W m^{-2}). Net radiation can be measured by four components
315   radiation sensors and is expressed as the difference between downward and upward shortwave ($R_{s\downarrow}$ and
316     $R_{s\uparrow}$, W m^{-2}) and longwave radiation ($R_{l\downarrow}$ and $R_{l\uparrow}$), specifically: $R_n = R_{s\downarrow} + R_{l\downarrow} - R_{s\uparrow} - R_{l\uparrow}$. Bowen

ratio ($Bo = \frac{SH}{LE}$) indicates the relative proportions of energy consumption between *SH* and *LE*. Typically,

Bo is high under dry conditions and low under wet conditions.

3 Results and discussions

3.1 The spatial-temporal variations of atmospheric meteorological variables
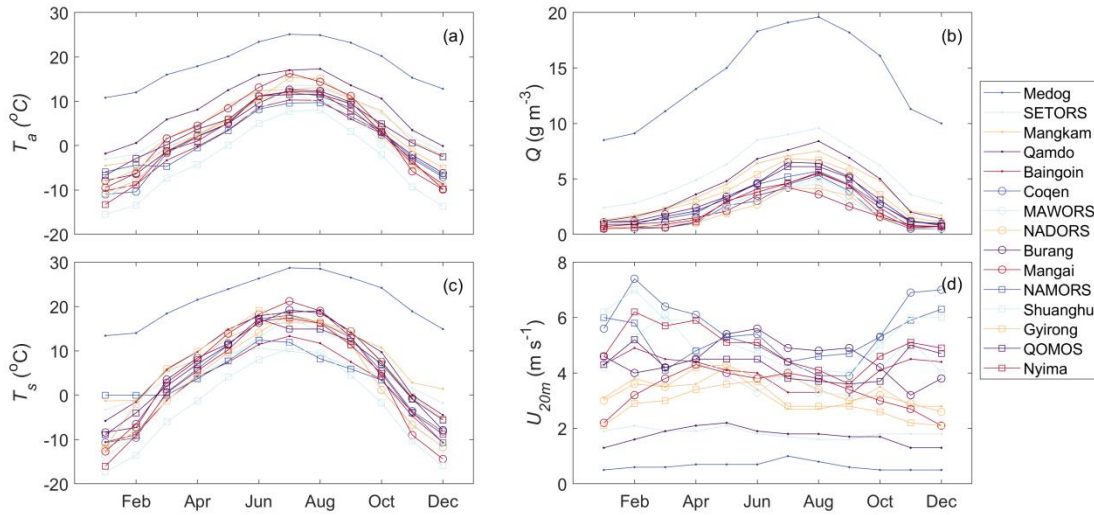
Figure 2. The seasonal variations of meteorological variables, including (a) air temperature (T_a), (b) air humidity (Q); (c) land surface temperature (T_s); (d) wind speed at 20 m height (U_{20m}).

The 15 stations are distributed across diverse environments and climates, resulting in considerable variations in the seasonal patterns of air temperature (T_a), air humidity (Q), wind speed (U_{20m}) and land surface temperature (T_s) (Figure 2 and Table 2). The details of seasonal variations of the monthly average and annual mean of air temperature, wind speed and absolute humidity at the 15 stations can be found in Table S2-S4. The annual average T_a, T_s, Q and U_{20m} span at ranges of -3.5~18.5 °C, -3.5~21.6 °C, 1.88~14.1 $g\,m^{-3}$ and 0.6~5.6 m s^{-1}, respectively. The annual average T_a shows strong positive correlations (*r*) with annual average T_s ($r = 0.99$, *p*<0.01) and downward long-wave radiation ($R_{l\downarrow}$, $r = 0.84$, *p*<0.01), and a notable negative correlation with downward short-wave radiation ($R_{s\downarrow}$, $r = -0.72$, *p*<0.01) (Figure S1). The high correlation with T_s indicates that strong LA coupling governs the spatial distribution of T_a, while the negative correlation with $R_{s\downarrow}$ reflects the impact of cloud cover, which reduces $R_{s\downarrow}$ but increases T_a. Additionally, the annual average T_a exhibits a significant negative correlation with elevation ($r = -0.92$, *p*<0.01). The highest annual average T_a (18.5°C) occurs at Medog station (820 m a.s.l.), while the lowest (−3.5°C) is observed at Shuanghu station (4947 m a.s.l.). Stations such as Qamdo (3307 m a.s.l.), SETORS (3327 m a.s.l.), Mangkam (3840 m a.s.l.), and Mangai (3073 m a.s.l.) have annual average values ranging from 5.2°C to 8.6°C, whereas stations above 4000 m have annual averages from −3.5°C to 3.9°C. Seasonal variations in T_a can also be influenced by climatic and environmental conditions. For example, despite similar elevations (around 3300 m a.s.l.) and low wind speeds (approximately 1.8 m s^{-1}), Qamdo shows larger annual value and amplitude in T_a than that in SETORS, and it may be attributed to the former's lower moisture condition as well as the strong "urban heat island" effect. Qamdo, having lower annual precipitation value, is located at a mountaintop grass land observation field in the city center, thus, relatively weak evaporated cooling and intense human

activities and infrastructure may contribute to Qamdo's elevated T_a. Similarly, in Baingoin and NAMORS, despite their proximity and similar elevations, NAMORS experiences higher T_a from October to February and lower temperatures from March to August. Such variations are likely influenced by the large lake (Nam Co), which has a cooling effect in summer and a warming effect in winter.

Table 2. The annual average meteorological variables, soil water contents (*SM 10cm* and *SM 160cm* indicate soil moisture at 10 cm and 160 cm, respectively), *NEE*, *GPP*, *Re*, *ET*, *EBR* and *Bo* at 15 stations.

| Sites	T_a (°C)	Q (g m^{-3})	U_{20m} (m s^{-1})	T_s (°C)	Prec (mm)	SM 10cm (%)	SM 160cm (%)	NEE (g C m^{-2}a^{-1})	GPP (g C m^{-2} a^{-1})	Re (g C m^{-2} a^{-1})	ET (mm)	EBR (-)	Bo (-)
Medog	18.5	14.1	0.6	21.6	2164	9 - 25	18 - 43	365	885	1193	571	1.04	0.46
SETORS	5.7	5.64	1.8	6.1	1053	32 - 42	20 - 50	-153	754	633	381	0.634	0.84
Mangkam	5.2	4.07	3.3	6.2	596	4 - 16	20 - 41	-121	454	192	345	0.683	1.09
Qamdo	8.6	4.3	1.7	9.0	456	4 - 14	8 - 19	-133	486	443	354	0.650	0.73
Baingoin	0.5	2.38	4.1	1.2	392	3 - 22	1 - 12	Nan	Nan	Nan	208	0.680	1.52
NAMORS	1.3	2.80	5.2	2.6	304	1 - 9	3 - 6	Nan	Nan	Nan	348	0.828	1.64
Shuanghu	-3.5	2.10	5.3	-3.5	246	1 - 10	9 - 38	-86	165	75	174	0.836	1.88
Gyirong	2.9	3.53	2.8	4.3	237	5 - 14	8 - 20	-58	249	189	218	0.641	2.35
QOMOS	3.9	2.98	4.3	5.6	196	2 - 9	2 - 3	Nan	Nan	Nan	115	0.797	4.11
Nyima	1.3	2.28	4.9	2.3	182	3 - 14	0 - 2	-13	56	36	194	0.631	2.02
Coqen	1.6	2.03	5.6	1.8	137	2 - 6	4 - 9	-15	146	260	155	0.821	3.94
MAWORS	0.8	2.23	4.3	1.0	107	1 - 9	1 - 29	-157	538	368	344	0.623	1.31
NADORS	2.4	1.88	3.5	3.0	64	12 - 48	20 - 50	-174	415	238	222	0.646	0.99
Burang	2.5	3.12	4.5	3.1	58	1 - 4	1 - 5	-65	100	33	121	0.659	4.10
Mangai	3.5	1.93	3.4	4.8	43	1 - 2	1 - 2	-3	69	20	76	0.747	8.32

Both air humidity (Q) and wind speed at a 20 m height (U_{20m}) at 15 stations show similar seasonal variations (Figures 2b and 2d). Generally, the seasonal patterns of Q and U_{20m} are influenced by the interaction of monsoon and westerly systems. Seasonally, the summer monsoon system leads to the lower values in U_{20m} and higher values in Q, while high values in U_{20m} and low values in Q during winter are coincident with the dominating westerly system. Spatially, Q decreases from southeast to northwest across the TP. Medog station, located in a subtropical forest climate, exhibits the highest annual average Q of 14.1 g m^{-3}. The higher group of annual average Q values are found at SETORS (5.61 g m^{-3}), Qamdo (4.28 g m^{-3}), and Mangkam (4.12 g m^{-3}), while the rest of the stations range from 1.74 to 3.67 g m^{-3}. Further, both the annual averages of Q and U_{20m} correlate with elevation, showing negative and positive correlations of -0.88 (p<0.01) and 0.83 (p<0.01), respectively (Figure S1). U_{20m} is the lowest in Medog, Qamdo, and SETORS, where wind speeds are generally under 2 m s^{-1}, primarily because of their locations in the southeast mountainous regions. Conversely, stations at higher elevations with more homogeneous landscapes, such as Nyima, Coqen, and Shuanghu, experience the highest wind speed.

Overall, the 15 stations reveal distinct spatial and seasonal variability in meteorological conditions across the TP, driven primarily by elevation and large-scale circulation systems. The combined effects of topography, monsoon and westerly influences, and local factors such as urbanization and lake regulation shape the observed gradients in temperature, humidity, and wind speed.

3.2 The spatial-temporal variations of liquid precipitation and soil water content

The wet-dry condition at each station is mostly correlated with liquid precipitation and soil water content (Table 2). The highest annual precipitation occurs in the southeastern TP, at stations like Medog, SETORS, Mangkam, and Qamdo, where the monsoon system dominates. The monsoon system can bring moist air into the plateau, resulting in annual precipitation values of 2164 mm in Medog, 1053 mm in SETORS, 596 mm in Mangkam, and 456 mm in Qamdo. In contrast, stations with low annual precipitation, such as Mangai, Burang, NADORS, and MAWORS, are located in the western and northern parts of the TP, where mid-latitude westerlies prevail, with annual precipitation below 120 mm. The rest seven stations in the central and western TP, where both westerly and monsoon systems interact, experience annual precipitation ranging from 120 mm to 400 mm. Specifically, Baingoin, NAMORS, and Shuanghu, located in the central TP, receive annual precipitation of between 200 mm and 400 mm, while Nyima, Coqen, Gyirong, and QOMOS receive100 mm to 200 mm per year. This pattern of high in the southeast and low in the northwest aligns with the Global Precipitation Measurement (GPM) product [*Li et al., 2021a*]. The spatial distribution of soil water content at depths of 10 cm and 160 cm generally mirrors the precipitation pattern, but they can be also influenced by soil properties and local conditions. For example, NADORS, situated near Bangong Co, exhibits the highest soil water content at 10 cm depth. At 160 cm depth, stations like Shuanghu, NADORS, MAWORS, and Gyirong show soil water content up to 0.20, indicating pronounced groundwater contribution. In contrast, Mangai, Burang, Coqen, and NAMORS have the lowest soil water contents.

Seasonally, liquid precipitation over the TP is primarily concentrated during the summer monsoon seasons, with peaks in July and August (Figure S3), consistent with findings from *Yang et al. [2023]* in central TP. *Chen et al. [2023]* observed that monthly precipitation in the Yarlung Tsangbo Grand Canyon exhibits two peaks, one in April and the other in August, which is also the case for SETORS and Medog. Diurnally, *Li et al. [2021b]* noted that summer precipitation over the TP often occurs in the afternoon and evening. However, the diurnal patterns vary markedly across the 15 stations (Figure 3). Precipitation frequency and amounts followed similar diurnal variations, with notable exceptions at Baingoin and MAWORS, where precipitation frequency peaked between 6:00 and 11:00, but the highest rainfall amounts occurred at 14:00. At westerly-dominated stations in the northern TP like Mangai, NADORS, MAWORS, and Shuanghu, precipitation peaks during the day and is minimal at night, though the timing of these peaks varies. In contrast, stations in mountainous regions—Medog, Mangkam, Qamdo, Nyima, and Gyirong—experience peak precipitation mostly at night, similar to findings in *Chen et al. [2023]* for the Yarlung Zangbo Grand Canyon. SETORS, QOMOS, and Coqen exhibit bimodal precipitation patterns, with peaks at night and in the late afternoon. Burang and NAMORS show higher precipitation in the first half of the day, with lower amounts later, and such patterns are probably related with the lake breeze circulation. Generally, daytime rainfall is probably driven by up-slope flows due to surface heating, while the monsoon nocturnal low-level jet may contribute to nighttime rainfall. Further, the local circulations of lake-land breeze and mountain-valley breeze can also modulate the water circulations and impact on the diurnal variation of precipitation.
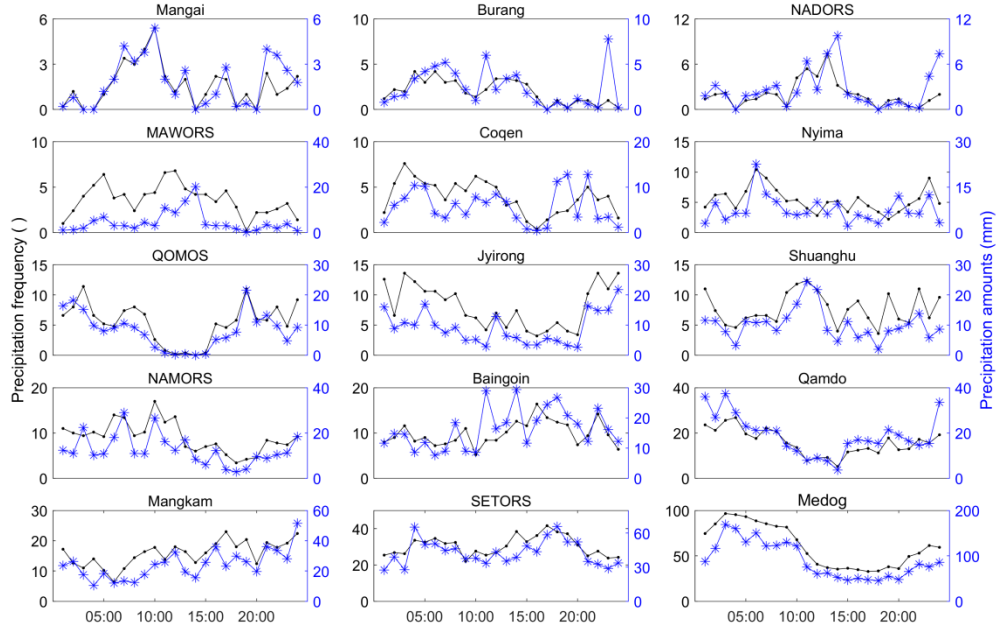
Figure 3. The diurnal variations of liquid precipitation amounts and frequency at 15 stations. Liquid precipitation frequency indicates the total times of liquid precipitation annually.

Overall, precipitation and soil moisture across the TP show a clear southeast–northwest gradient, decreasing from humid monsoon regions to arid westerly-dominated areas. Seasonal and diurnal variations reflect the combined influence of the summer monsoon, local topography, and mesoscale circulations such as mountain–valley and lake–land breezes. These spatial and temporal patterns highlight strong hydroclimatic heterogeneity and its control on regional LA coupling.

3.3 The spatial-temporal variations of energy flux

Net radiation (R_n) provides the energy source for LA energy and material exchange, and is mainly divided into three components: ground heat flux (G), *SH*, and *LE*. R_n generally shows positive values in its seasonal variations, indicating that the ground surface acts as a heat source relative to the overlying atmosphere. R_n peaks in June or July and reaches its lowest in December or January. SETORS and Gyirong have monthly R_n values of greater than 90 W m², while Baingoin and Mangai have values of below 70 W m². The other stations show values of between 70 and 90 W m², which are similar to those reported in previous studies, 4 stations over the TP and 4 stations in the lower reaches of the Yangtze River region [*Yao et al., 2024*]. Details for the seasonal variation of monthly net radiation and monthly ground heat flux and their annual means at the 15 stations can be found in Table S5-S6. Further, heat storage occurs mainly from March to August, peaking around June, while heat release is most remarkable from October to February, with the largest release in December. The annual average of monthly G ranges from -0.01 W m² at Qamdo to 2.39 W m² at NADORS. The close-to-zero G values suggest minimal impact of ground heat storage on the energy budget at an annual scale, while the dominating positive values suggest a warming trend in the ground, aligning with global warming and the rise in land surface temperature *[Duan and Xiao, 2015; Oku et al., 2006; Zhang et al., 2023*].
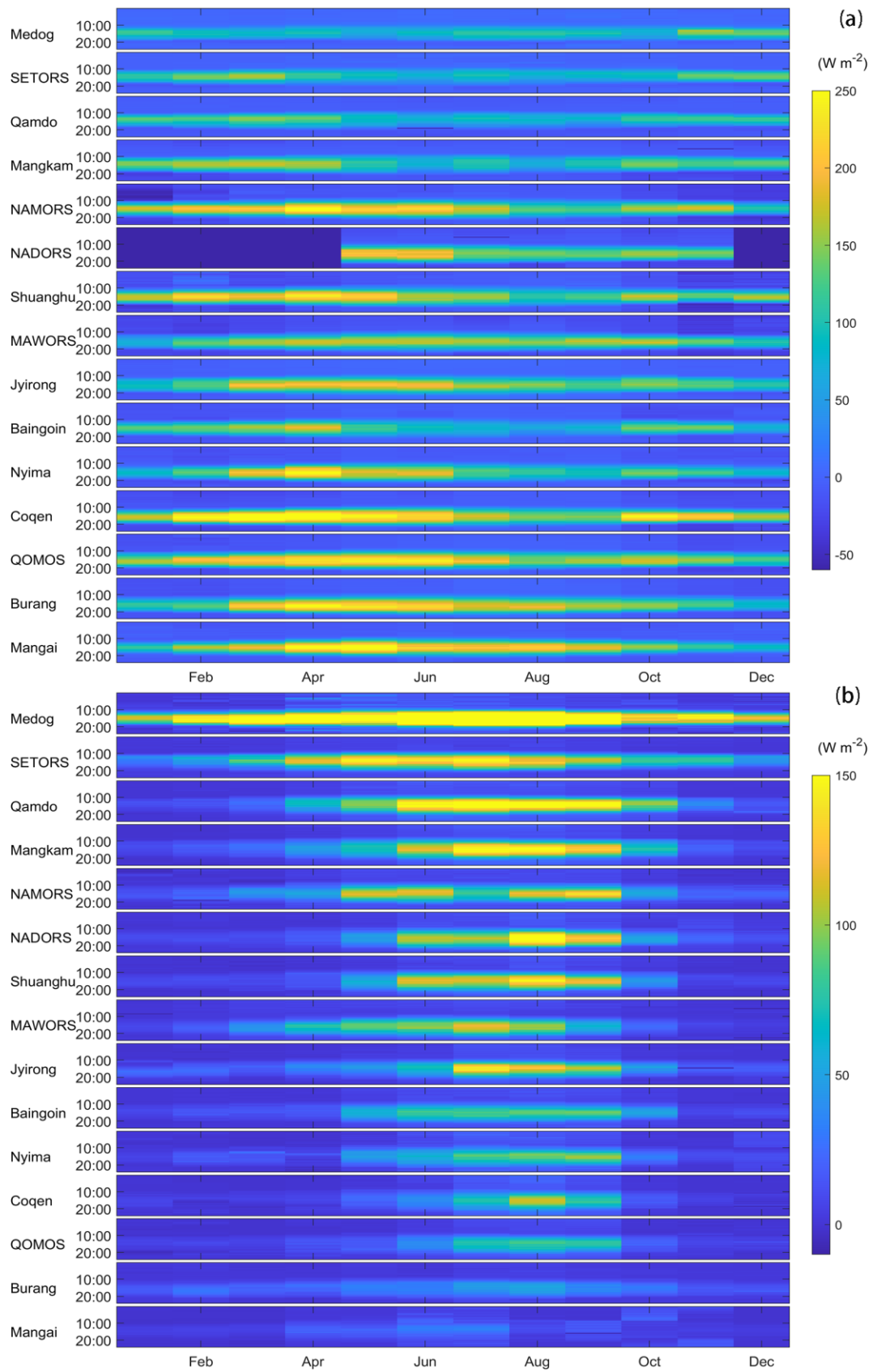
Figure 4. The heat maps for averaged diurnal and seasonal variations of sensible heat flux (a) and latent heat flux (b) at 15 stations.

Turbulent heat fluxes, including *SH* and *LE*, exhibit clear diurnal and seasonal variations (Figure 4), consistent with previous studies on the TP [*Ma et al.*, 2005; *Zhong et al.*, 2019a]. In addition, the seasonal evolution of monthly averaged diurnal *SH* and *LE* can be found in Figure S4-S5. *SH* peaks during the pre-monsoon months of April and May, and is lowest in the cold months of December and January. Stations with sufficient water availability, such as Medog, SETORS, Mangkam, Qamdo, Baingoin, MAWORS, and NADORS, have total annual *SH* values ranging from 269 to 356 W m^{-2}. The first five stations receive high precipitation, while the latter two have substantial soil moisture supply. Other stations have total annual *SH* fluxes exceeding 400 W m^{-2}, with QOMOS and Coqen reporting the highest annual values of 582 W m^{-2} and 626 W m^{-2}, respectively. *LE* peaks during the monsoon seasons (July to August) and is not apparent throughout the cold months. Specifically, the total annual *LE* is only 61.3 W m^{-2} at the extremely dry Mangai station, while Medog records monthly *LE* values all exceeding 29 W m^{-2}. Spatially, *LE* is showing decreasing pattern from the southeast wet regions to the northwest dry regions. As shown in Table 1, the *Bo* reflects the energy distribution between *SH* and *LE*. Medog, SETORS, and Qamdo in the southeast have *Bo* values of less than 1, indicating dominant heat consumption through the *LE*, while Mangai, Burang, and QOMOS in the northern and western regions have *Bo* ratios greater than 4, suggesting the dominant role of *SH*.

The *EBR* is the ratio of turbulent energy fluxes (*SH* + *LE*) to available energy (R_n - *G*). The average *EBR* across the 15 stations is approximately 0.73, ranging from 0.62 to 1.04, with 11 stations between 0.6 and 0.8, while Medog exceeds 1 (Table 2). These values are consistent with results from global eddy flux sites [Wilson et al., 2002]. Imperfect energy balance closure can arise from several factors [Foken, 2008; Mauder et al., 2020], including footprint mismatch, instrumental biases, unaccounted energy storage, flux losses at different frequencies, and neglected advection. The influence of these factors likely varies among sites according to their surface heterogeneity and terrain complexity. A detailed site-level attribution of *EBR* differences requires further analysis and will be addressed in future work.

Following the LA interaction theories, *SH* (*LE*) are primarily influenced by land-atmosphere temperature gradients ($\Delta T = T_s - T_a$) or water vapor deficit ($\Delta E = e_s - e_a$, where e_s and e_a are the saturation vapor pressure and the actual vapor pressure respectively), wind speed (*U*), soil moisture at 10 cm and 80 cm, land surface temperature (T_s) and net radiation (R_n), etc [*Wang et al., 2017*]. The correlation coefficients between *SH* (*LE*) and the related variables can be found in Table S7, and the dominating factors for LA turbulent flux are pronouncedly different under dry and wet stations, where energy-related variables are most important in water-sufficient conditions, while water-related variables show dominant role in water-shortage conditions. For example, wet stations such as Medog, SETORS, Mangkam, and Qamdo, which receive substantial precipitation and maintain high soil moisture, exhibit stronger correlations of *LE* with R_n and T_s than with soil moisture. In contrast, dry stations such as QOMOS, Nyima, Coqen, and Burang, characterized by low precipitation and limited soil moisture, show higher correlations of *LE* with soil moisture at 10 cm than with other variables. Mangai, an extremely dry station with annual precipitation value of only 43.2 mm and very low soil moisture conditions (0.01-0.02), has the smallest annual *ET* value and no obvious correlations with all the variables. In NADORS, the annual *ET* has a value of 222.4 mm, significantly higher than the annual precipitation amount of 64 mm, and the volumetric water

content at 80 cm can reach up to 0.3, suggesting a substantial impact of groundwater supply. Thus, soil moisture and R_n have comparable high correlation coefficients in NADORS.

The correlation coefficients between *SH* (*LE*) and related environment variables under conditions of all stations, wet stations (Medog, SETORS, Mangkam, and Qamdo) and dry stations (QOMOS, Nyima, Coqen, Burang) are grouped in Figure 5. For all stations included, *SH* variations are primarily driven by ΔT, followed by R_n and T_s, with correlation coefficients of 0.57, 0.55 and 0.34, respectively (Figure 5a). Further, *SH* has a positive correlation with wind speed and a negative correlation with soil moisture. The correlation coefficients show large diversity under dry and wet conditions, with generally lower values in wet stations than those in dry stations. For example, the averaged correlation coefficients between *SH* and $\Delta T/R_n/T_s$ under dry stations are 0.63/0.65/0.44 while those values (0.32/0.40/0.13) are much smaller under wet conditions. Wind speed has weaker correlation with *SH*. but in MAWORS and Medog, the correlation coefficients could approach to 0.5. In NAMORS, there is a negative correlation between wind speed and *SH*. These phenomenons may be related with the local circulations of mountain-valley and lake-land breezes, which may lead to synchronized and opposite variations in such conditions.
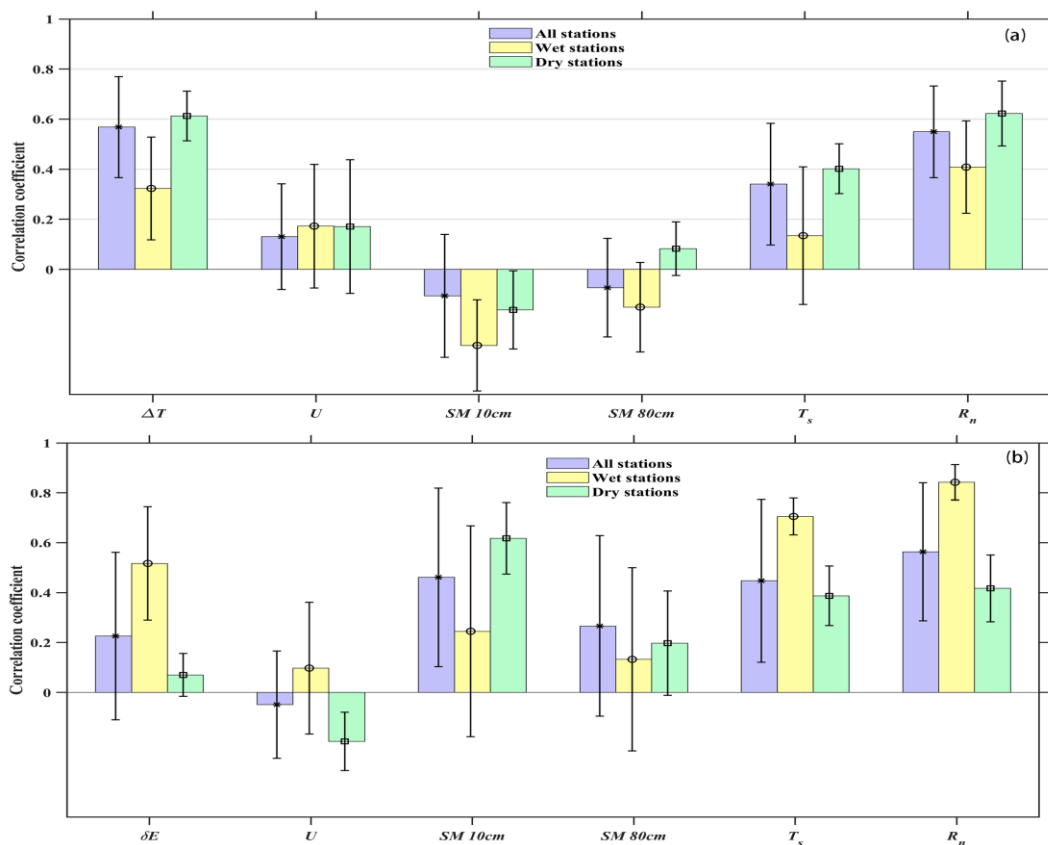
Figure 5. The correlation coefficients between sensible heat flux (a), latent heat flux (b) and related environmental variables at a temporal resolution of hourly under conditions of all stations, wet stations and dry stations, respectively. The statistical significance of the correlation coefficients for each station is provided in Table S7.

The correlations between *LE* and environmental variables are more complex (Table S7 and Figure 5b). The three paramount factors are R_n, T_s and soil moisture at 10 cm, with correlation coefficients of 0.56, 0.46, 0.45, respectively. For wet stations, the most important variables are energy related variables (R_n and T_s). Stations such as Medog, Mangkam, SETORS, Qamdo, Gyirong, and NADORS follow this pattern, with the first four stations influenced by high precipitation and the latter two by soil water content. *ΔE* represents the difference between the actual and saturation vapor pressure, indicating the atmospheric moisture deficit. The saturation vapor pressure increases exponentially with temperature—by about 6–7% per degree Celsius—so warmer air can hold substantially more water vapor than cooler air. Thus, *ΔE* shows remarkable high correlations at Medog and SETORS. At stations like Burang, Nyima, MAWORS, and Coqen, the most influential variable is soil moisture, followed by R_n and T_s. Thus, both energy and water availability play dominant roles. At extremely dry station of Mangai, most of the monthly *LE* values are close to zero, and none of the variations show obvious correlations with *LE*. For QOMOS, the largest correlation with *LE* is seen with soil moisture at 10 cm, suggesting that water availability plays a more critical role in *ET* than energy availability in this region.

In a brief summary, turbulent fluxes of *SH* and *LE* display clear spatial and seasonal patterns, with the Bowen ratio reflecting this energy partitioning. Correlation analyses reveal that *SH* is primarily driven by temperature gradients, whereas *LE* is controlled by energy-related factors in wet regions and by soil moisture availability in dry regions, highlighting the contrasting mechanisms of LA coupling across the TP.

3.4 The seasonal variations of *NEE*, *GPP* and *Re*

The seasonal variations of daily *NEE*, *GPP*, and *Res* averaged over the observational period show remarkable differences across sites, and the sites with relatively good vegetation coverage follow a single-peak distribution pattern, i.e. SETORS, Qamdo, Mangkam, etc., but the other sites, including Burang, Nyima, Coqen, Mangai, show weak or nearly non seasonal variations (Figure 6 and Table 2). The carbon absorption and release are determined by vegetation photosynthesis process and ecosystem respiration. The seasonal variation of carbon fluxes follow the vegetation growth, with highest values during the summer peak growing seasons. For example, stations with substantial vegetation growth, such as SETORS, Qamdo, Mangkam, NADORS, and MAWORS, exhibit higher peaks and fluctuations in *NEE*, *GPP*, and *Re*. The first three stations benefit from high precipitation, while the latter two stations receive considerable shallow soil water supply from surrounding lakes or glaciers. These five stations exhibit strong carbon sink capacities, with *NEE* values all smaller than -120 g C m^{-2} during the growing season. Specifically, NADORS shows the largest *NEE* value of -174 g C m^{-2} from May to October, while SETORS has the highest daily *NEE* values, exceeding 6 g C m^{-2} d^{-1}. Similarly, *GPP* and *Re* values at the 5 stations all exceed 400 g C m^{-2} and 190 g C m^{-2}, with SETORS having the highest *GPP* and *Re* values of 754 g C m^{-2} and 633 g C m^{-2}, respectively, due to its favorable temperature and water conditions for vegetation growth. In water-limited regions like Mangai and Nyima, carbon fluxes fluctuations are minimal. Daily *NEE* values remain below 0.5 g C m^{-2} d^{-1}, even during the growing season. The total annual *NEE* values are -3.2 g C m^{-2} and -12.8 g C m^{-2} in Mangai and Nyima, respectively. *GPP* and *Re* values are also low, with annual totals below 70 g C m^{-2} for *GPP* and 40 g C m^{-2} for *Re*. The smallest annual *GPP* value is 56 g C m^{-2} at Nyima, and the smallest annual *Re* value is 20 g C m^{-2} at Mangai. Although

543 annual *NEE* values at SETORS and MAWORS are relatively similar, SETORS has much larger
544 *GPP* and *Re* values because of the efficient water supply and warm climate. In contrast, *[Wang et*
545 *al., 2021]* reported NADORS with average *GPP* value of 1.60 g C m^{-2} d^{-1} and average *Re* value of
546 0.71 g C m^{-2} d^{-1} during growing season of 2014-2015, while these values (2.93 g C m^{-2} d^{-1} for *GPP*
547 and 1.35 g C m^{-2} d^{-1} for *Re*) are much larger during growing season of 2021-2022 in our estimation.
548 In addition, the maximum net carbon uptake has a value of -2.1 g C m^{-2} d^{-1} in MAWORS during
549 2015-2016 *[Wang et al., 2021],* however, the largest *NEE* exchange value is -2.6 g C m^{-2} d^{-1} in our
550 measurements. Thus, it may indicate the improvement of vegetation status in the two western
551 stations during the past 10 years *[Zhong et al., 2019b].*
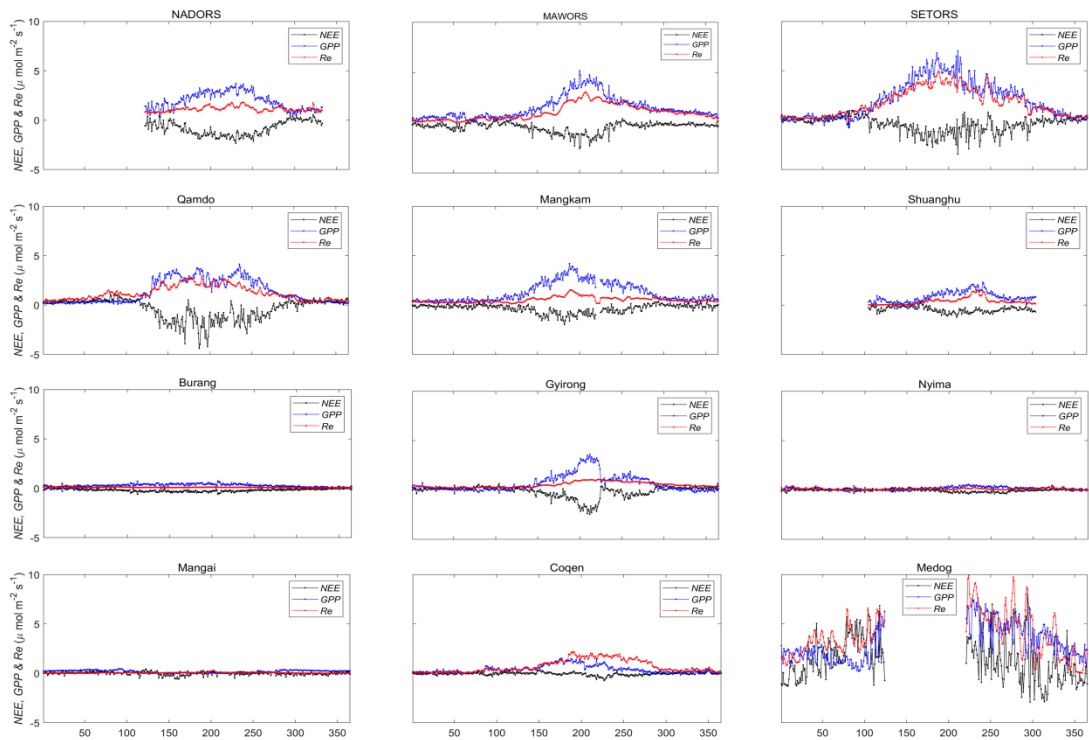
552
553 **Figure 6**. The seasonal variations in *NEE, GPP*, *Re* across different sites. The negative *NEE* values
554 indicated a net uptake of CO$_2$. The black, blue and red lines stand for daily *NEE, GPP* and *Re*,
555 respectively.

556 　　　　The annual *NEE* values are negative at 11 out of 12 stations, with exceptions at Medog (Table
557 1). The annual *NEE* values at the stations of Qamdo, SETORS, Mangkam, MAWORS and
558 NADORS all smaller than -120 g C, coincident with stations with higher *ET* annual values,
559 suggesting the significance of water-carbon coupling in land-atmosphere interaction process. At
560 stations of Shuanghu, Burang, Jyirong, the annual *NEE* values are between -50 g C and -100 g C
561 and the rest stations of Nyima and Mangai have annual *NEE* values of close to carbon neutral. At
562 Medog, despite substantial carbon absorption during the daytime, remarkable carbon release at night
563 caused by soil respiration leads to large carbon release. Mangai, with sparse vegetation, functions
564 nearly as carbon neutral. An obvious drastic variation of *NEE* values during August at Gyirong
565 station can be found and it corresponds to a soil drought event caused by water deficit. The water
566 deficit event results in decrease in *NEE* and *LE* and obvious increase in T_s and *SH*. Notably, carbon
567 absorption primarily occurs during summer growing seasons of May to September and function as
568 carbon neutral during winter seasons. The spatial distribution of annual *NEE* values generally follow

the distribution of water conditions, where sufficient water can promote vegetation growth, allowing photosynthesis to absorb more CO_2 than respiration releases [*Wang et al., 2021; Wang et al., 2023*].

Global forests have been widely recognized as carbon sinks [*Hubau et al.*, 2020; *Pan et al., 2024*]. Medog station, located in the Yarlung Zangbo River valley, is surrounded by subtropical forests and has an annual *NEE* value of 365 g C, indicating that the land cover acts as an obvious carbon source. Studies have indicated that tropical forests can become carbon sources due to factors such as deforestation, soil respiration exceeding photosynthesis, lingering droughts, and extreme warming [*Gatti et al., 2021; Mills et al., 2023; Xie et al., 2016*]. During a severe drought in the summer of 2013 in a subtropical forest in China, the ecosystem switched to a net carbon source by late August [*Xie et al., 2016*]. Mills et al. [2023] reported that tropical forests, following deforestation and degradation, can shift from carbon sinks to carbon sources. Similarly, the Medog station, located in a hot and humid region with complex terrain, has experienced recent site disturbance associated with station construction in the southern area, leading to partial vegetation removal and soil exposure. These disturbances likely enhanced soil and microbial respiration, resulting in net carbon release. Moreover, topographic shading caused by surrounding steep terrain reduces solar radiation exposure, thereby constraining photosynthesis [Wang et al., 2021; Wang et al., 2023]. The pronounced seasonal variation in *GPP* at this site (Figure 6) is mainly driven by monsoonal climatic conditions—*GPP* peaks during the warm and moist summer months when radiation and temperature are favorable but declines markedly during the cooler and cloudier pre- and post-monsoon periods (Figure S6). Although *NEE* values can be obviously negative during the daytime due to photosynthesis, obvious and long-lasting ecosystem respiration at night leads to a net carbon release (Figure S6).

Across the TP, carbon fluxes exhibit clear spatial and seasonal variability linked to vegetation cover and water availability. Stations with abundant precipitation or shallow groundwater act as strong carbon sinks, e.g. SETORS, NADORS, while arid sites such as Mangai and Nyima remain nearly carbon neutral. In contrast, the Medog station functions as a carbon source, likely due to vegetation disturbance, soil respiration, and complex topographic and climatic conditions that limit photosynthetic uptake.

4 Summary

The establishment of a comprehensive observation and research platform marks a remarkable advancement in understanding land-atmosphere water, heat and CO_2 flux across diverse stations. The platform features standardized configurations at each station, including an EC system, a 20 m PBL tower measuring wind, temperature, and humidity across five layers, soil moisture and temperature probes at five depths, energy budget probes for radiation components and soil heat flux, a thermal infrared temperature probe, a barometer, and a rain gauge. It covers a range of landscapes such as alpine steppe, alpine meadow, grassland, bare ground, forest, and desert. The observation platform aims to provide long-term, standardized, high-quality data on land-atmosphere interaction processes over the TP, with a particular focus on the data-scarce regions of the western TP. The extensive hydrometeorological dataset offers initial insights into the spatial and temporal variations of meteorological conditions, liquid precipitation, and turbulent fluxes. Diurnal precipitation

patterns reveal three types: peak at night, peak during the day, and bimodal peaks. While liquid precipitation can distinguish between water-limited and energy-limited regions, soil moisture—both from surface and deeper layers—also plays a key role in *ET*, as seen in stations like NADORS and Shuanghu. *NEE* fluxes are near zero at bare ground stations, show notable carbon release in forested areas under construction, and function as carbon sinks in most alpine meadows and alpine steppe sites. This platform is critical for supporting scientific research and sustainable development. However, challenges remain in capturing data from remote and heterogeneous regions, as well as limitations in current technologies. Scaling flux towers for global models remains difficult, highlighting the need for robust interpolation and validation techniques. Additionally, further investigation is required to understand the impacts of land-use changes, such as deforestation and reforestation, on turbulent heat fluxes and their feedback to the climate system.

Competing interests

The authors declare that they have no conflict of interests.

Author contribution

BBW and YMM jointly led the writing of this article and were responsible for the establishment and maintenance of the experimental sites and instrumentation. BBW took the lead in dataset consolidation, processed the data into the standardized format described in this study, and drafted the manuscript in collaboration with all co-authors. ZYH, XL, WQM, XLC, CBH, ZPX, YYW, MSL, BM, XDS, WML, and ZLC contributed to the maintenance of the observation systems, data analysis, and provided critical feedback and revisions to the manuscript.

Data availability statement

The hourly dataset including air temperature, air humidity, wind speed, land surface temperature, soil moisture, downward shortwave radiation, downward longwave radiation, upward shortwave radiation, upward longwave radiation, sensible heat flux, latent heat flux, Net ecosystem change can be downloaded freely in the Tibetan Plateau Data Center. The DOI of the dataset is https://doi.org/10.11888/Atmos.tpdc.302428. The data can be referenced by Wang and Ma (2025). The web link is https://data.tpdc.ac.cn/en/disallow/e8032ff8-2437-4363-876f-2af4e4558a4d. New collected data will be properly processed and added to this web link in the Tibetan Plateau Data Center.

Acknowledgement

References

André, J.-C., J.-P. Goutorbe, and A. Perrier (1986), HAPEX—MOBILHY: A Hydrologic Atmospheric Experiment the Study of Water Budget and Evaporation Flux at the Climatic Scale, *Bulletin of the American Meteorological Society*, *67*(2), 138-144, doi:https://doi.org/10.1175/1520-0477-67.2.138.

Baldocchi, D. (2014), Measuring fluxes of trace gases and energy between ecosystems and the atmosphere – the state and future of the eddy covariance method, *Global Change Biology*, *20*(12), 3600-3609, doi:https://doi.org/10.1111/gcb.12649.

Bei, N., L. Zhao, J. Wu, X. Li, T. Feng, and G. Li (2018), Impacts of sea-land and mountain-valley circulations on the air pollution in Beijing-Tianjin-Hebei (BTH): A case study, *Environmental Pollution*, *234*, 429-438, doi:https://doi.org/10.1016/j.envpol.2017.11.066.

Chen, X., D. Cao, Y. Liu, X. Xu, and Y. Ma (2023), An observational view of rainfall characteristics and evaluation of ERA5 diurnal cycle in the Yarlung Tsangbo Grand Canyon, China, *Quarterly Journal of the Royal Meteorological Society*, *149*(753), 1459-1472, doi:https://doi.org/10.1002/qj.4468.

Duan, A., and Z. Xiao (2015), Does the climate warming hiatus exist over the Tibetan Plateau?, *Scientific Reports*, *5*(1), 13711, doi:10.1038/srep13711.

Foken, T. (2008), THE ENERGY BALANCE CLOSURE PROBLEM: AN OVERVIEW, *Ecological Applications*, *18*(6), 1351-1367, doi:https://doi.org/10.1890/06-0922.1.

Friedlingstein, P., et al. (2022), Global Carbon Budget 2022, *Earth Syst. Sci. Data*, *14*(11), 4811-4900, doi:10.5194/essd-14-4811-2022.

Gatti, L. V., et al. (2021), Amazonia as a carbon source linked to deforestation and climate change, *Nature*, *595*(7867), 388-393, doi:10.1038/s41586-021-03629-6.

Gentine, P., A. Massmann, B. R. Lintner, S. Hamed Alemohammad, R. Fu, J. K. Green, D. Kennedy, and J. Vilà-Guerau de Arellano (2019), Land–atmosphere interactions in the tropics – a review, *Hydrol. Earth Syst. Sci.*, *23*(10), 4171-4197, doi:10.5194/hess-23-4171-2019.

Gerken, T., T. Biermann, W. Babel, M. Herzog, Y. Ma, T. Foken, and H.-F. Graf (2014), A modelling investigation into lake-breeze development and convection triggering in the Nam Co Lake basin, Tibetan Plateau, *Theoretical and Applied Climatology*, *117*(1), 149-167, doi:10.1007/s00704-013-0987-9.

Goutorbe, J. P., et al. (1997), An overview of HAPEX-Sahel: a study in climate and desertification, *Journal of Hydrology*, *188-189*, 4-17, doi:https://doi.org/10.1016/S0022-1694(96)03308-2.

Halldin, S., S. E. Gryning, L. Gottschalk, A. Jochum, L. C. Lundin, and A. A. Van de Griend (1999), Energy, water and carbon exchange in a boreal forest landscape — NOPEX experiences, *Agricultural and Forest Meteorology*, *98-99*, 5-29, doi:https://doi.org/10.1016/S0168-1923(99)00148-3.

Huang, J., et al. (2023), Global Climate Impacts of Land-Surface and Atmospheric Processes Over the Tibetan Plateau, *Reviews of Geophysics*, *61*(3), e2022RG000771, doi:https://doi.org/10.1029/2022RG000771.

Hubau, W., et al. (2020), Asynchronous carbon sink saturation in African and Amazonian tropical forests, *Nature*, *579*(7797), 80-87, doi:10.1038/s41586-020-2035-0.

Li, G., Z. Yu, W. Wang, Q. Ju, and X. Chen (2021a), Analysis of the spatial Distribution of precipitation and topography with GPM data in the Tibetan Plateau, *Atmospheric Research*, *247*, 105259, doi:https://doi.org/10.1016/j.atmosres.2020.105259.

Li, L., R. Zhang, P. Wu, M. Wen, and J. Duan (2020), Roles of Tibetan Plateau vortices in the heavy rainfall over southwestern China in early July 2018, *Atmospheric Research*, *245*, 105059, doi:https://doi.org/10.1016/j.atmosres.2020.105059.

687 Li, P., K. Furtado, T. Zhou, H. Chen, and J. Li (2021b), Convection-permitting modelling improves
688 simulated precipitation over the central and eastern Tibetan Plateau, *Quarterly Journal of the Royal*
689 *Meteorological Society*, *147*(734), 341-362, doi:https://doi.org/10.1002/qj.3921.

690 Liu, S., et al. (2018), The Heihe Integrated Observatory Network: A Basin-Scale Land Surface Processes
691 Observatory in China, *Vadose Zone Journal*, *17*(1), 180072, doi:https://doi.org/10.2136/vzj2018.04.0072.

692 Lü, D., Z. Chen, G. Wang, J. Chen, J. Ji, Y. Li, and H. Chen (1997), Inner Mongolia Semi-Arid Grassland
693 Soil-Vegetation-Atmosphere Interaction, *Climatic and Environmental Research*, *2*(3), 199-209,
694 doi:10.3878/j.issn.1006-9585.1997.03.01.

695 Ma, N., and Y. Zhang (2022), Increasing Tibetan Plateau terrestrial evapotranspiration primarily driven
696 by precipitation, *Agricultural and Forest Meteorology*, *317*, 108887,
697 doi:https://doi.org/10.1016/j.agrformet.2022.108887.

698 Ma, Y., S. Fan, H. Ishikawa, O. Tsukamoto, T. Yao, T. Koike, H. Zuo, Z. Hu, and Z. Su (2005), Diurnal
699 and inter-monthly variation of land surface heat fluxes over the central Tibetan Plateau area, *Theoretical*
700 *and Applied Climatology*, *80*(2), 259-273, doi:10.1007/s00704-004-0104-1.

701 Ma, Y., et al. (2020), A long-term (2005–2016) dataset of hourly integrated land–atmosphere interaction
702 observations on the Tibetan Plateau, *Earth Syst. Sci. Data*, *12*(4), 2937-2957, doi:10.5194/essd-12-2937-
703 2020.

704 Ma, Y., Y. Wang, and C. Han (2018), Regionalization of land surface heat fluxes over the heterogeneous
705 landscape: from the Tibetan Plateau to the Third Pole region, *International Journal of Remote Sensing*,
706 *39*(18), 5872-5890, doi:10.1080/01431161.2018.1508923.

707 Ma, Y., et al. (2024), Dataset of spatially extensive long-term quality-assured land–atmosphere
708 interactions over the Tibetan Plateau, *Earth Syst. Sci. Data*, *16*(6), 3017-3043, doi:10.5194/essd-16-
709 3017-2024.

710 Ma, Y., et al. (2023), Comprehensive study of energy and water exchange over the Tibetan Plateau: A
711 review and perspective: From GAME/Tibet and CAMP/Tibet to TORP, TPEORP, and TPEITORP, *Earth-*
712 *Science Reviews*, *237*, 104312, doi:https://doi.org/10.1016/j.earscirev.2023.104312.

713 Ma, Y. M., S. C. Kang, L. P. Zhu, B. Q. Xu, L. D. Tian, and T. D. Yao (2008), TIBETAN OBSERVATION
714 AND RESEARCH PLATFORM Atmosphere-Land Interaction over a Heterogeneous Landscape,
715 *Bull.amer.meteor.soc*, *89*(10), 1487-1492.

716 Massman, W. J., and X. Lee (2002), Eddy covariance flux corrections and uncertainties in long-term
717 studies of carbon and energy exchanges, *Agricultural and Forest Meteorology*, *113*(1), 121-144,
718 doi:https://doi.org/10.1016/S0168-1923(02)00105-3.

719 Mauder, M., M. Cuntz, C. Drüe, A. Graf, C. Rebmann, H. P. Schmid, M. Schmidt, and R. Steinbrecher
720 (2013), A strategy for quality and uncertainty assessment of long-term eddy-covariance measurements,
721 *Agricultural and Forest Meteorology*, *169*, 122-135, doi:https://doi.org/10.1016/j.agrformet.2012.09.006.

722 Mauder, M., and T. Foken (2006), Impact of post-field data processing on eddy covariance flux estimates
723 and energy balance closure, *Meteorologische Zeitschrift*, *15*(6), 597-609.

724 Mauder, M., T. Foken, and J. Cuxart (2020), Surface-Energy-Balance Closure over Land: A Review,
725 *Boundary-Layer Meteorology*, *177*(2), 395-426, doi:10.1007/s10546-020-00529-6.

726 Mills, M. B., et al. (2023), Tropical forests post-logging are a persistent net carbon source to the
727 atmosphere, *Proceedings of the National Academy of Sciences*, *120*(3), e2214462120,
728 doi:doi:10.1073/pnas.2214462120.

729 Oku, Y., H. Ishikawa, S. Haginoya, and Y. Ma (2006), Recent Trends in Land Surface Temperature on
730 the Tibetan Plateau, *Journal of Climate*, *19*(12), 2995-3003, doi:https://doi.org/10.1175/JCLI3811.1.

731 Pan, Y., Birdsey, R.A., Phillips, O.L. et al. The enduring world forest carbon sink. Nature 631, 563–569
732 (2024)

733 Qi, Y., D. Wei, H. Zhao, and X. Wang (2021), Carbon Sink of a Very High Marshland on the Tibetan
734 Plateau, *Journal of Geophysical Research: Biogeosciences*, *126*(4), e2020JG006235,
735 doi:https://doi.org/10.1029/2020JG006235.

736 Santanello, J. A., et al. (2018), Land–Atmosphere Interactions: The LoCo Perspective, *Bulletin of the*
737 *American Meteorological Society*, *99*(6), 1253-1272, doi:https://doi.org/10.1175/BAMS-D-17-0001.1.

738 Sellers, P., et al. (1995), The Boreal Ecosystem–Atmosphere Study (BOREAS): An Overview and Early
739 Results from the 1994 Field Year, *Bulletin of the American Meteorological Society*, *76*(9), 1549-1577,
740 doi:https://doi.org/10.1175/1520-0477(1995)076<1549:TBESAO>2.0.CO;2.

741 Sellers, P. J., F. G. Hall, G. Asrar, D. E. Strebel, and R. E. Murphy (1992), An overview of the First
742 International Satellite Land Surface Climatology Project (ISLSCP) Field Experiment (FIFE), *Journal of*
743 *Geophysical Research: Atmospheres*, *97*(D17), 18345-18371, doi:https://doi.org/10.1029/92JD02111.

744 Seo, Y.-W., and K.-J. Ha (2022), Changes in land-atmosphere coupling increase compound drought and
745 heatwaves over northern East Asia, *npj Climate and Atmospheric Science*, *5*(1), 100,
746 doi:10.1038/s41612-022-00325-8.

747 Suni, T., et al. (2015), The significance of land-atmosphere interactions in the Earth system—iLEAPS
748 achievements and perspectives, *Anthropocene*, *12*, 69-84,
749 doi:https://doi.org/10.1016/j.ancene.2015.12.001.

750 Turetsky, M. R., et al. (2020), Carbon release through abrupt permafrost thaw, *Nature Geoscience*, *13*(2),
751 138-143, doi:10.1038/s41561-019-0526-0.

752 Twine, T. E., W. P. Kustas, J. M. Norman, D. R. Cook, P. R. Houser, T. P. Meyers, J. H. Prueger, P. J.
753 Starks, and M. L. Wesely (2000), Correcting eddy-covariance flux underestimates over a grassland,
754 *Agricultural and Forest Meteorology*, *103*(3), 279-300, doi:https://doi.org/10.1016/S0168-
755 1923(00)00123-4.

756 Wang, Shuzhou, and Yaoming (2011), Characteristics of Land-Atmosphere Interaction Parameters over
757 the Tibetan Plateau, *Journal of Hydrometeorology*.

758 Wang, B., Y. Ma, W. Ma, and Z. Su (2017), Physical controls on half-hourly, daily, and monthly turbulent
759 flux and energy budget over a high-altitude small lake on the Tibetan Plateau, *Journal of Geophysical*
760 *Research: Atmospheres*, *122*(4), 2289-2303, doi:https://doi.org/10.1002/2016JD026109.

761 Wang, B., Ma, Y. (2025). Meteorological variables and eddy fluxes at 15 land-atmosphere interaction
762 stations over the Tibetan Plateau (May-2021 to July 2023). National Tibetan Plateau / Third Pole
763 Environment Data Center. https://doi.org/10.11888/Atmos.tpdc.302428.

764 Wang, Y., J. Xiao, Y. Ma, J. Ding, X. Chen, Z. Ding, and Y. Luo (2023), Persistent and enhanced carbon
765 sequestration capacity of alpine grasslands on Earth's Third Pole, *Science Advances*, *9*.

766 Wang, Y., J. Xiao, Y. Ma, Y. Luo, Z. Hu, F. Li, Y. Li, L. Gu, Z. Li, and L. Yuan (2021), Carbon fluxes and
767 environmental controls across different alpine grassland types on the Tibetan Plateau, *Agricultural and*
768 *Forest Meteorology*, *311*, 108694, doi:https://doi.org/10.1016/j.agrformet.2021.108694.

769 Wei, D., Y. Qi, Y. Ma, X. Wang, W. Ma, T. Gao, L. Huang, H. Zhao, J. Zhang, and X. Wang (2021), Plant
770 uptake of CO_2 outpaces losses from permafrost and plant respiration on the Tibetan Plateau,
771 *Proceedings of the National Academy of Sciences*, *118*(33), e2015283118,
772 doi:doi:10.1073/pnas.2015283118.

773 Wilson, K., et al. (2002), Energy balance closure at FLUXNET sites, *Agricultural and Forest*
774 *Meteorology*, *113*(1), 223-243, doi:https://doi.org/10.1016/S0168-1923(02)00109-0.

23

775 Wu, G., and Y. Zhang (1998), Tibetan Plateau Forcing and the Timing of the Monsoon Onset over South
776 Asia and the South China Sea, *Monthly Weather Review*, *126*(4), 913-927.
777 Wu, G., et al. (2023), An Integrated Research Plan for the Tibetan Plateau Land–Air Coupled System
778 and Its Impacts on the Global Climate, *Bulletin of the American Meteorological Society*, *104*(1), E158-
779 E177, doi:https://doi.org/10.1175/BAMS-D-21-0293.1.
780 Wutzler, T., A. Lucas-Moffat, M. Migliavacca, J. Knauer, K. Sickel, L. Šigut, O. Menzer, and M.
781 Reichstein (2018), Basic and extensible post-processing of eddy covariance flux data with REddyProc,
782 *Biogeosciences*, *15*(16), 5015-5030, doi:10.5194/bg-15-5015-2018.
783 Xie, Z., L. Wang, B. Jia, and X. Yuan (2016), Measuring and modeling the impact of a severe drought
784 on terrestrial ecosystem CO_2 and water fluxes in a subtropical forest, *Journal of Geophysical Research:*
785 *Biogeosciences*, *121*(10), 2576-2587, doi:https://doi.org/10.1002/2016JG003437.
786 Xu, X., and L. Chen (2006), Advances of the Study on Tibetan Plateau Experiment of Atmospheric
787 Sciences, *Journal of Applied Meteorological Science*, *17*(6), 756-772.
788 Yang, K., et al. (2023), Cross-sectional rainfall observation on the central-western Tibetan Plateau in the
789 warm season: System design and preliminary results, *Science China Earth Sciences*, *66*(5), 1015-1030,
790 doi:10.1007/s11430-022-1081-4.
791 Yang, K., T. Koike, H. Ishikawa, O. Kim, X. Li, H. Liu, S. Liu, M. A. Yaoming, and J. Wang (2008),
792 Turbulent Flux Transfer over Bare-Soil Surfaces; Characteristics and Parameterization, *Journal of*
793 *Applied Meteorology and Climatology*(1), 47.
794 Yao, N., Y. Ma, B. Wang, J. Zou, J. Sun, and Z. Xie (2024), A comparative study of the land–atmosphere
795 energy and water exchanges over the Tibetan Plateau and the Yangtze River Region, *Atmospheric and*
796 *Oceanic Science Letters*, *17*(2), 100447, doi:https://doi.org/10.1016/j.aosl.2023.100447.
797 Ye, D.-Z., and G.-X. Wu (1998), The role of the heat source of the Tibetan Plateau in the general
798 circulation, *Meteorology and Atmospheric Physics*, *67*(1), 181-198, doi:10.1007/BF01277509.
799 Yu, G.-R., Z. Chen, and Y.-P. Wang (2024), Carbon, water and energy fluxes of terrestrial ecosystems in
800 China, *Agricultural and Forest Meteorology*, *346*, 109890,
801 doi:https://doi.org/10.1016/j.agrformet.2024.109890.
802 Yuan, L., X. Chen, Y. Ma, C. Han, B. Wang, and W. Ma (2024), Long-term monthly 0.05° terrestrial
803 evapotranspiration dataset (1982–2018) for the Tibetan Plateau, *Earth Syst. Sci. Data*, *16*(2), 775-801,
804 doi:10.5194/essd-16-775-2024.
805 Yuan, L., Y. Ma, X. Chen, Y. Wang, and Z. li (2021), An Enhanced MOD16 Evapotranspiration Model
806 for the Tibetan Plateau During the Unfrozen Season, *Journal of Geophysical Research: Atmospheres*,
807 *126*, doi:10.1029/2020JD032787.
808 Zhang, C., D.-H. Qin, and P.-M. Zhai (2023), Amplification of warming on the Tibetan Plateau, *Advances*
809 *in Climate Change Research*, *14*(4), 493-501, doi:https://doi.org/10.1016/j.accre.2023.07.004.
810 Zhang, Y., N. Wagner, K. Goergen, and S. Kollet (2024), Summer evapotranspiration-cloud feedbacks in
811 land-atmosphere interactions over Europe, *Climate Dynamics*, doi:10.1007/s00382-024-07475-w.
812 Zhao, L., Y. Li, X. Zhao, S. Xu, Y. Tang, G. Yu, S. Gu, M. Du, and Q. Wang (2005), Comparative study
813 of the net exchange of CO_2 in 3 types of vegetation ecosystems on the Qinghai-Tibetan Plateau, *Chinese*
814 *Science Bulletin*, *50*(16), 1767-1774, doi:10.1360/04wd0316.
815 Zhong, L., Y. Ma, Z. Hu, Y. Fu, Y. Hu, X. Wang, M. Cheng, and N. Ge (2019), Estimation of hourly land
816 surface heat fluxes over the Tibetan Plateau by the combined use of geostationary and polar-orbiting
817 satellites, *Atmos. Chem. Phys.*, *19*(8), 5529-5541, doi:10.5194/acp-19-5529-2019.

818   Zhu, L., Z. Meng, F. Zhang, and P. M. Markowski (2017), The influence of sea- and land-breeze

819   circulations on the diurnal variability in precipitation over a tropical island, *Atmos. Chem. Phys.*, *17*(21),

820   13213-13232, doi:10.5194/acp-17-13213-2017.

821
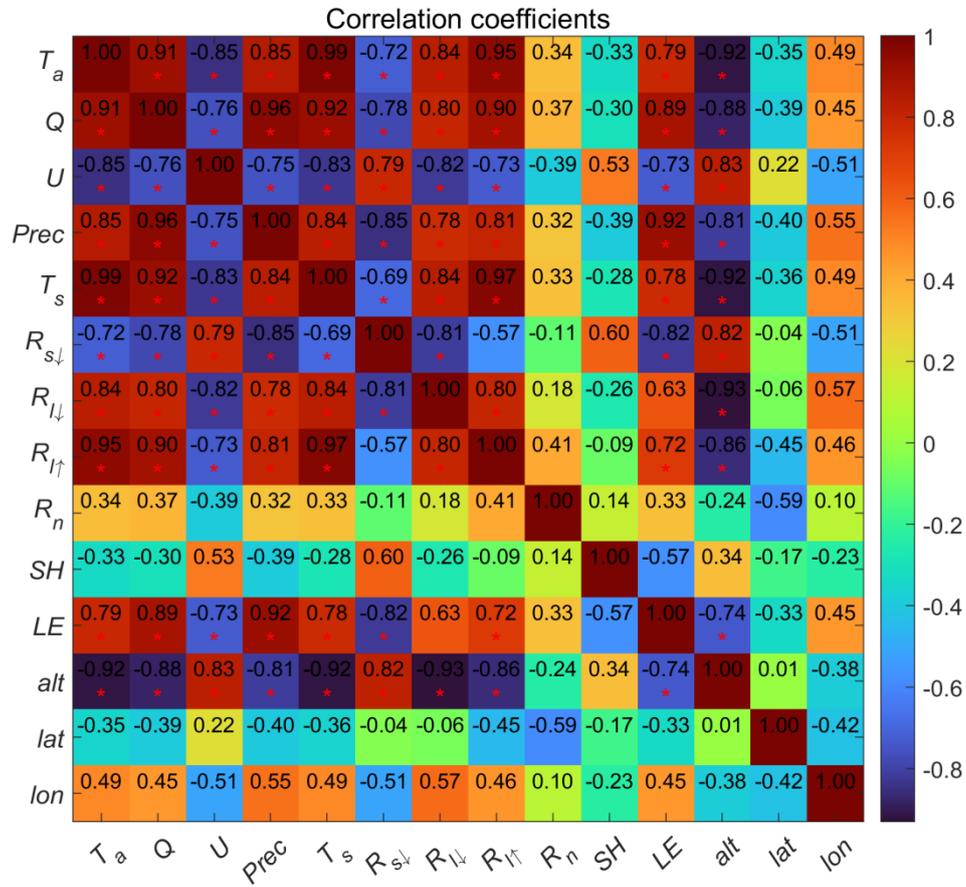
Figure S1. The heat map of correlation coefficients for air temperature (T_a), air humidity (Q), wind speed (U), precipitation (*Prec*), land surface temperature (T_s), downward short wave radiation ($R_{s\downarrow}$), downward long wave radiation ($R_{l\downarrow}$), upward longwave radiation ($R_{l\uparrow}$), net radiation (R_n), sensible heat flux (*SH*), latent heat flux (*LE*), altitude (*alt*), latitude (*lat*), longitude (*lon*) for 15 stations. An asterisk (*) indicates that the correlation coefficient is statistically significant at the 0.01 level.
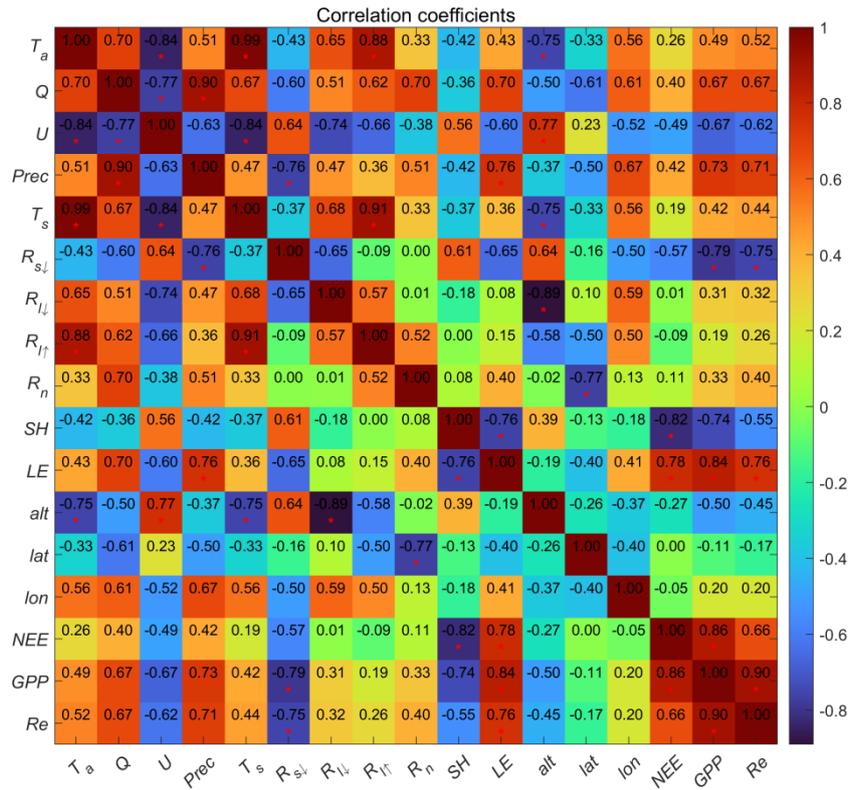
Figure S2. The heat map of correlation coefficients for air temperature (T_a), air humidity (Q), wind speed (U), precipitation *(Prec)*, land surface temperature (T_s), downward short wave radiation ($R_{s\downarrow}$), downward long wave radiation ($R_{l\downarrow}$), upward longwave radiation ($R_{l\uparrow}$), net radiation (R_n), sensible heat flux (SH), latent heat flux (LE), net ecosystem exchange (NEE), gross primary productivity (GPP) and ecosystem respiration (Re), altitude *(alt)*, latitude *(lat)*, longitude *(lon)* for 12 stations with an exception of Baingoin, QOMOS, NAMORS. An asterisk (*) indicates that the correlation coefficient is statistically significant at the 0.01 level.
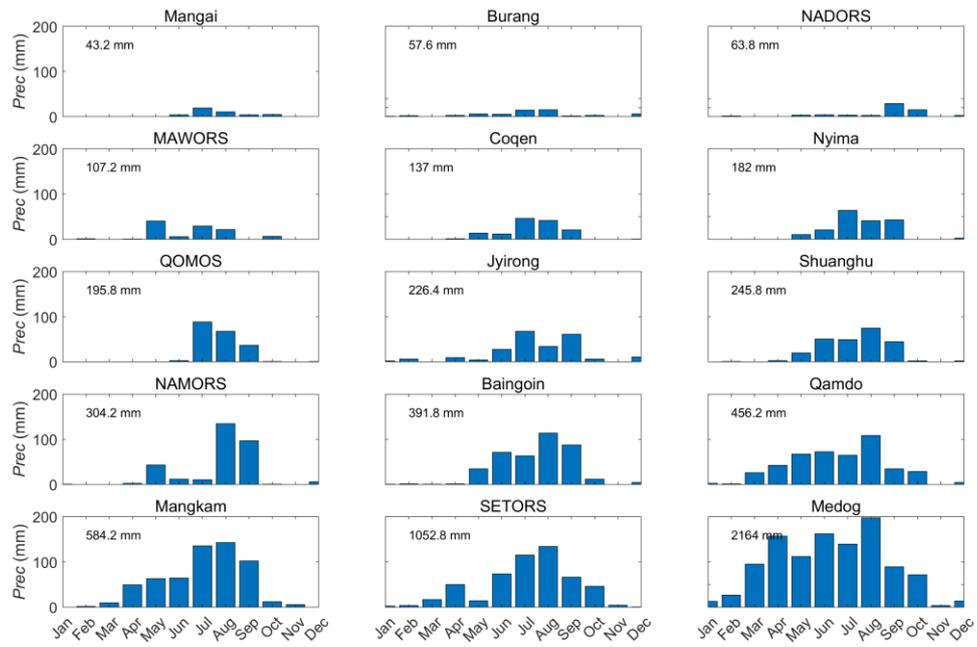
Figure S3. The seasonal variations of monthly precipitation (*Prec*) at 15 stations, with the annual precipitation value marked at each subplot.
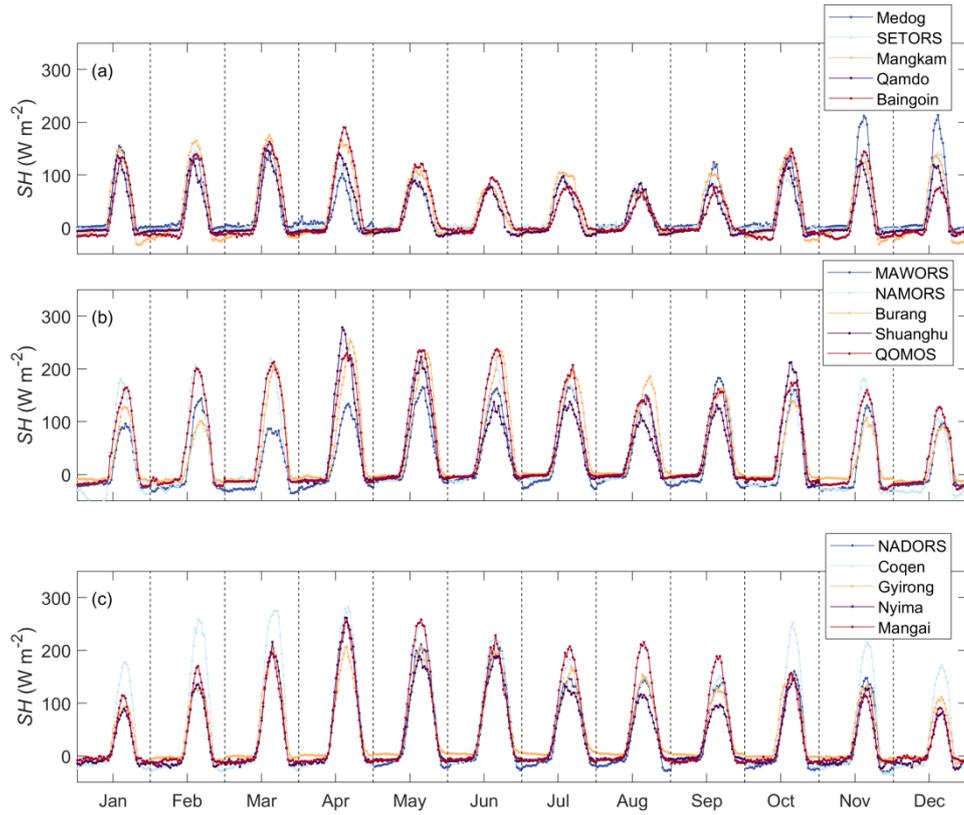
Figure S4. The seasonal variations of averaged *SH* for Medog, SETORS, Mangkam, Qamdo, Baingoin in (a), MAWORS, NAMORS, Burang, Shuanghu, QOMOS in (b), and NADORS, Coqen, Gyirong, Nyima and Mangai in (c).
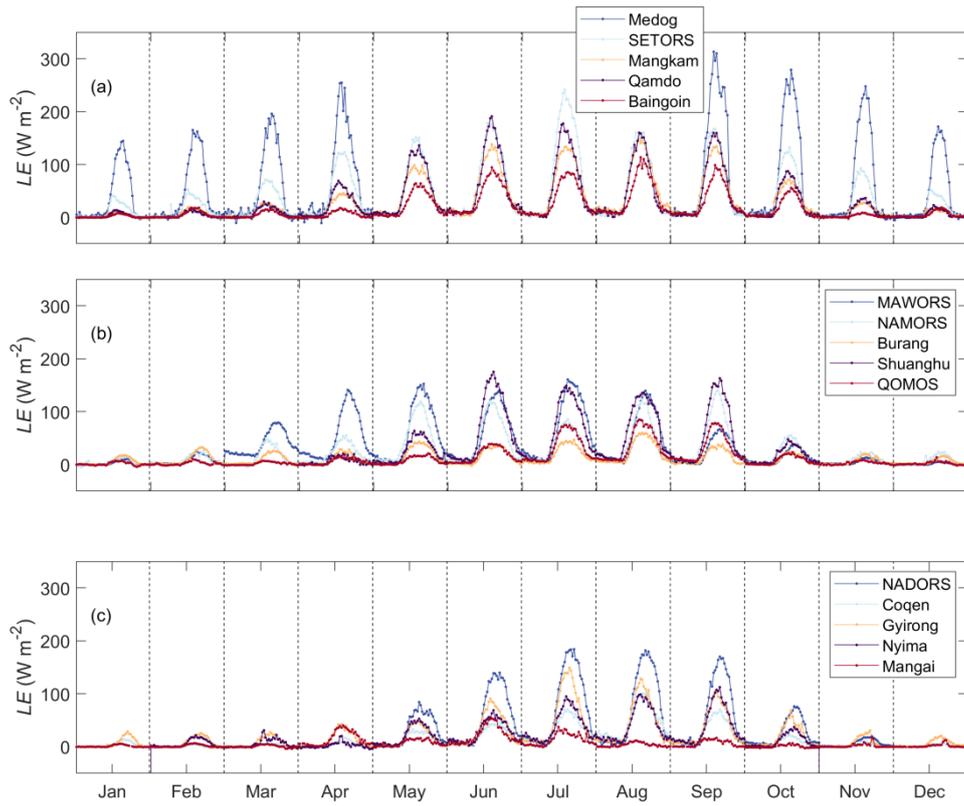
Figure S5. The seasonal variations of averaged *LE* for Medog, SETORS, Mangkam, Qamdo, Baingoin in (a), MAWORS, NAMORS, Burang, Shuanghu, QOMOS in (b), and NADORS, Coqen, Gyirong, Nyima and Mangai in (c).
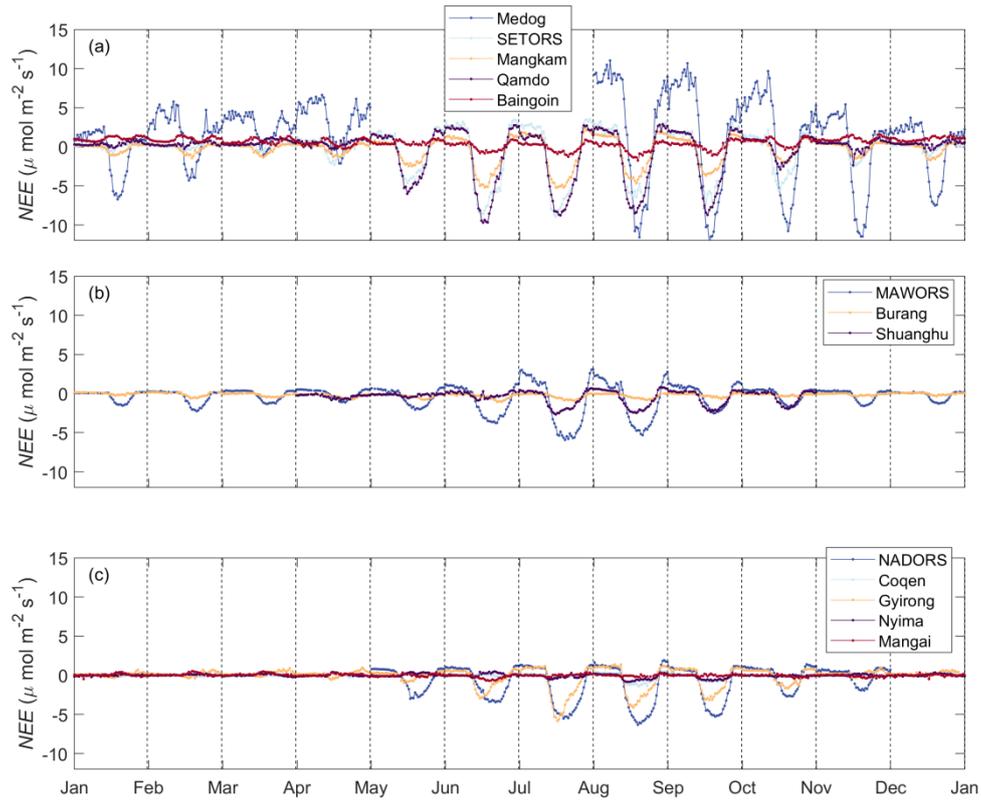
Figure S6. The seasonal variations of averaged *NEE* for Medog, SETORS, Mangkam, Qamdo, Baingoin in (a), MAWORS, Burang, Shuanghu in (b), and NADORS, Coqen, Gyirong, Nyima and Mangai in (c).

Table S1. The duration of observation and the percentage values of meteorological variables and eddy flux at 15 stations.

Sites	Start of the observational data series	End of the observational data series	Meteorological variables	Eddy flux
Medog	2021-04-18	2023-10-16	100%	60%
SETORS	2021-04-10	2023-10-29	100%	86%
Mangkam	2021-05-12	2023-10-16	100%	100%
Qamdo	2021-05-08	2023-10-17	100%	100%
Baingoin	2021-04-10	2023-06-28	100%	100%
NAMORS	2021-05-09	2023-11-01	90%	88%
Shuanghu	2021-04-11	2023-07-01	100%	100%
Gyirong	2021-04-23	2023-07-10	100%	68%
QOMOS	2021-04-18	2023-07-12	88%	77%
Nyima	2021-04-14	2023-03-15	100%	76%
Coqen	2021-05-01	2023-11-01	81%	100%
MAWORS	2021-05-24	2023-07-23	100%	57%
NADORS	2021-04-26	2023-08-06	100%	100%
Burang	2021-04-27	2023-11-08	100%	100%
Mangai	2021-04-12	2023-07-18	58%	47%

Table S2. The seasonal variation of monthly air temperature and its annual mean at the 15 stations

T_a (℃)	Jan	Feb	Mar	Apr	May	Jun	Jul	Aug	Sep	Oct	Nov	Dec	Mean
NADORS	-11.9	-10.1	-0.6	3.8	7.6	11.3	16.5	15.4	11.2	3.5	-3.7	-12	2.4
Baingoin	-12.6	-11.8	-1.7	0.1	4.1	9.1	10.4	9.4	5.7	4.4	-4.3	-11	0.5
SETORS	-3.6	-3.7	2.6	5.0	8.8	12.3	13.8	12.8	10.4	8.2	2.2	-1.8	5.7
Qamdo	-3.2	-1.5	6.9	7.8	12.7	16.0	17.3	16.3	13.2	12.0	3.2	-0.2	8.6
Coqen	-11	-10.4	-1.7	1.9	5.0	11.1	12.3	11.5	8.2	4.4	-2.9	-8.7	1.6
Gyirong	-10.7	-8.3	0.8	4.0	6.4	10.7	12.1	11.5	9.6	5.5	-1.1	-5.6	2.9
Medog	10.6	10.8	16.6	18.7	20.6	23.2	25.5	24.0	23.2	20.9	15.6	12.1	18.5
MAWORS	-9.8	-10.1	0.4	3.6	5.9	7.6	11.4	9	9.2	0.1	-6.2	-11	0.8
NAMORS	-6.7	-8.7	-4.0	-1.9	4.3	8.7	10	8.8	5.8	5.3	-2.5	-4.7	1.3
Burang	-9.2	-9.4	-0.6	3.8	5.7	9.8	12.9	12.2	10.2	4.3	-2.8	-8.4	2.5
Shuanghu	-18.1	-16.2	-6.2	-4.3	0.8	5.8	7.8	7.0	3.1	-0.2	-9.6	-15.9	-3.5
QOMOS	-6.7	-4.7	1.3	5.0	6.5	11.5	11.3	11.2	9.2	5.8	1.2	-3.4	3.9
Nyima	-19.1	-12.2	-1.2	1.0	5.2	11.2	12.4	11.5	7.8	5.2	-3.7	-13.8	1.3
Mangai	-9.5	-9.1	2.7	4.8	9.1	12.2	17.1	14.4	11.2	4.2	-5.8	-9.9	3.5
Mangkam	-6.2	-5.7	2.6	3.7	9.9	12.4	12.7	12.4	9.9	8.5	0.8	-2.2	5.2

Table S3. The seasonal variation of monthly wind speed and its annual mean at the 15 stations

U_{20m} (m s^{-1})	Jan	Feb	Mar	Apr	May	Jun	Jul	Aug	Sep	Oct	Nov	Dec	Mean
NADORS	2.3	3.2	3.8	4.1	4.0	3.9	4.1	3.6	3.1	3.4	2.9	1.8	3.5
Baingoin	3.4	4.6	4.8	4.5	3.8	4.2	3.3	3.3	3.2	4.9	4.4	3.5	4.1
SETORS	1.9	2.1	1.9	1.8	2.1	1.8	1.8	1.6	1.6	1.8	1.9	1.8	1.8
Qamdo	1.3	1.7	1.8	1.9	2.2	1.9	1.8	1.8	1.6	1.6	1.3	1.4	1.7
Coqen	5.6	7.4	6.4	6.1	5.3	5.4	4.3	4.0	3.8	5.7	6.8	6.2	5.6
Gyirong	1.4	2.5	2.9	3.4	3.5	3.6	3.0	2.8	2.6	2.7	2.1	2.2	2.8
Medog	0.5	0.6	0.5	0.7	0.5	0.5	0.9	0.5	0.5	0.3	0.3	0.4	0.6
MAWORS	3.4	3.3	5.3	3.3	2.6	2.6	2.6	2.4	2.5	3.0	3.2	2.5	4.3
NAMORS	5.4	3.6	4.6	4.5	5.2	5.2	4.5	4.8	4.1	5.7	5.8	6.2	5.2
Burang	4.4	4.0	3.7	4.2	5.2	5.7	5.0	5.2	4.7	4.3	3.1	4.5	4.5
Shuanghu	5.0	6.7	6.8	6.0	4.8	4.7	4.3	4.1	3.9	5.6	6.3	4.6	5.3
QOMOS	4.3	5.4	4.3	4.4	4.4	4.5	3.7	3.7	3.5	3.6	5.1	4.7	4.3
Nyima	1.8	4.8	5.7	5.9	5.1	5.1	4.5	4.1	3.6	5.2	5.0	3.6	4.9
Mangai	2.2	3.0	3.9	4.3	4.1	3.8	3.9	3.7	3.4	3.1	2.6	1.9	3.4
Mangkam	2.9	4.0	3.4	3.1	4.2	3.2	2.6	3.0	2.7	3.7	2.9	3.2	3.3

Table S4. The seasonal variation of monthly absolute humidity and its annual mean at the 15 stations

Q (g m^{-3})	Jan	Feb	Mar	Apr	May	Jun	Jul	Aug	Sep	Oct	Nov	Dec	Mean
NADORS	0.7	0.6	0.6	1.0	2.3	2.4	3.9	3.3	3.3	1.3	0.6	0.9	1.88
Baingoin	0.7	0.7	0.6	1.1	3.2	4.5	4.5	5.8	4.2	2.1	0.7	1.0	2.38
SETORS	2.3	2.2	3.3	4.9	6.7	8.9	8.7	9.7	7.6	6.4	3.9	2.7	5.64
Qamdo	1.3	1.3	2.1	4.0	5.2	7.3	7.1	8.5	6.7	4.4	2.0	1.5	4.3
Coqen	0.5	0.5	0.6	1.0	2.6	3.0	4.3	5.1	3.9	1.4	0.4	0.7	2.03
Gyirong	1.3	1.3	2.2	3.2	4.2	5.7	6.7	6.8	5.8	4.0	1.4	1.4	3.53
Medog	8.4	8.2	11.1	13.5	15.6	18.5	19.0	19.2	18.0	16.5	11.7	9.6	14.1
MAWORS	0.7	0.9	1.4	2.1	3.2	3.5	4.6	4.1	2.3	1.7	1.1	0.8	2.23
NAMORS	0.9	0.9	1.3	1.8	3.7	4.8	4.8	5.8	4.3	2.5	1.0	1.2	2.8
Burang	1.1	1.1	1.5	2.4	3.7	4.7	6.4	6.3	5.5	2.9	1.1	1.1	3.12
Shuanghu	0.5	0.6	0.6	1.0	2.6	4.0	4.1	5.0	3.4	1.6	0.5	0.7	2.1
QOMOS	0.9	0.8	1.6	2.2	3.7	4.9	6.4	6.4	5.0	3.5	1.3	0.9	2.98
Nyima	0.7	0.7	0.6	1.1	3.0	3.8	4.5	5.7	4.1	1.6	0.5	1.0	2.28
Mangai	0.7	0.7	1.3	1.6	1.9	4.0	4.5	3.6	2.5	1.6	0.8	0.7	1.93
Mangkam	1.3	1.5	2.1	3.8	4.9	6.6	6.8	7.4	6.1	4.7	2.4	1.8	4.07

Table S5. The seasonal variation of monthly net radiation and its annual mean at the 15 stations

R_n(W m^{-2})	Jan	Feb	Mar	Apr	May	Jun	Jul	Aug	Sep	Oct	Nov	Dec	Mean
NADORS	19.4	39.2	61.2	83.3	103.4	129.9	125.4	121.2	95.3	48.2	17.2	6.1	70.8
Baingoin	12.7	26.2	61.6	82.6	110.6	115.1	110.6	92.0	82.9	48.5	12.9	-3.6	62.7
SETORS	56.1	66.3	88.6	108.5	115.7	117.0	134.1	116.1	98.5	78.9	74.5	57.7	92.7
Qamdo	26.4	38.1	65.9	90.4	107.6	130.8	144.8	125.7	108.6	76.0	41.2	25.9	81.8
Coqen	32.2	53.3	92.8	99.5	116.2	119.9	125.2	117.6	95.5	61.7	35.7	21.8	81.0
Gyirong	19.9	68.2	94.9	112.5	133.0	155.2	156.3	153.9	127.5	91.0	49.6	33.1	99.6
Medog	52.0	61.3	74.3	80.2	87.6	109.6	139.6	117.3	110.1	69.7	65.4	55.2	85.2
MAWORS	27.6	48.5	75.5	109.5	131.6	128.5	125.8	113.2	82.8	53.6	28.2	14.4	78.2
NAMORS	NaN	NaN	NaN	117.6	144.2	150.6	132.9	128.1	119.4	72.5	43.0	13.7	76.8
Burang	20.0	45.3	95.4	120.5	138.0	138.8	133.9	126.9	96.1	67.1	37.3	3.2	85.2
Shuanghu	16.0	39.9	69.3	89.0	120.2	135.7	130.1	118.3	97.7	39.7	9.5	6.1	72.6
QOMOS	32.8	59.3	74.8	92.5	106.7	116.1	128.5	118.8	106.2	70.6	34.7	16.2	79.8
Nyima	27.2	47.4	84.7	106.6	122.3	136.1	127.9	108.6	100.4	60.5	29.2	8.4	79.9
Mangai	18.9	37.9	67.7	82.5	105.9	102.5	109.6	82.4	80.9	50.5	28.8	7.2	64.4
Mangkam	30.1	51.6	79.1	98.4	119.9	124.2	136.8	126.6	111.7	78.8	38.6	24.6	85.0

Table S6. The seasonal variation of monthly ground heat flux and its annual mean at the 15 stations.

G (W m^{-2})	Jan	Feb	Mar	Apr	May	Jun	Jul	Aug	Sep	Oct	Nov	Dec	Mean
NADORS	-5.9	-3.0	3.4	7.2	13.6	14.7	10.3	2.9	2.4	-2.1	-5.6	-9.2	2.39
Baingoin	-6.6	-3.8	4.0	6.2	7.6	8.3	5.0	-0.1	-1	-2.8	-6.9	-7.9	0.17
SETORS	-3.6	-2.2	0.2	0.9	3.5	5.6	5.3	0.7	-0.5	-1.7	-3.4	-4.6	0.02
Qamdo	-4.4	-0.7	2.2	1.0	2.0	3.9	6.0	1.7	-1.0	-1.8	-4.3	-4.7	-0.01
Coqen	-3.0	-1.8	3.9	3.3	6.9	9.1	5.6	2.7	0.4	-1.6	-3.9	-4.2	1.45
Gyirong	-3.8	-0.8	2.3	2.2	6.4	6.2	3.6	2.2	0.5	-0.6	-3.1	-3.8	0.94
Medog	-1.7	-0.8	1.4	3.0	2.6	1.9	3.0	0.7	0.9	-1.3	-2.6	-3.1	0.33
MAWORS	-2.3	-2.0	2.9	5.2	6.2	9.1	5.3	1.8	1.0	-3.0	-3.7	-4.2	1.36
NAMORS	-2.0	-2.0	2.0	3.9	5.6	7.4	3.7	1.6	-0.5	-0.6	-3.7	-4.3	0.93
Burang	-3.4	-2.6	3.4	3.3	5.6	6.5	5.1	1.5	0.5	-0.9	-3.1	-5.5	0.87
Shuanghu	-4.4	-2.6	1.3	3.7	7.8	10.3	9.0	2.8	0.9	-1.3	-4.8	-5.1	1.47
QOMOS	-2.1	-0.2	3.6	3.1	4.9	6.2	3.8	2.5	2.4	-0.8	-2.2	-3.3	1.49
Nyima	-2.8	-0.6	4.2	4.8	6.7	9.8	4.7	1.4	-0.4	-2.0	-4.1	-4.4	1.44
Mangai	-2.6	-0.7	3.3	5.5	4.9	4.0	5.1	3.1	0.9	-2.0	-4.0	-4.5	1.08
Mangkam	-2.1	-0.4	2.3	1.5	7.5	7.5	6.3	2.5	1.6	1.1	-2.2	-1.1	2.04

Table S7. The correlation coefficients (r) between SH (LE) and related meteorological and environmental variables. An asterisk (*) indicates that the correlation coefficient is statistically significant at the 0.05 level.

r	$SH \sim \Delta T$	$SH \sim U$	$SH \sim SM10$	$SH \sim SM80$	$SH \sim T_s$	$SH \sim R_n$	$LE \sim \Delta E$	$LE \sim U$	$LE \sim SM10$	$LE \sim SM80$	$LE \sim T_s$	$LE \sim R_n$
Medog	0.654*	0.623*	-0.570*	-0.450*	0.675*	0.752*	0.705*	0.580*	-0.459*	-0.410*	0.631*	0.787*
SETORS	0.092	-0.026	-0.055	-0.074	-0.125	0.483*	0.783*	-0.008	0.227*	0.503*	0.782*	0.936*
Mangkam	0.483*	0.227*	-0.323*	-0.079	0.062	0.297*	0.208*	-0.161*	0.648*	-0.038	0.673*	0.789*
Qamdo	0.150*	-0.064*	-0.270*	0.005	0.006	0.184*	0.399*	0.020	0.541*	0.453*	0.767*	0.884*
Baingoin	0.630*	0.199*	-0.319*	-0.380*	0.122*	0.402*	0.216*	0.038	0.752*	0.627*	0.395*	0.541*
NAMORS	0.852*	-0.128	-0.092	-0.192*	0.657*	0.647*	-0.005	-0.069	0.618*	-0.106	0.436*	0.699*
Shuanghu	0.545*	0.144	-0.026	0.046	0.222*	0.445*	0.329*	-0.276*	0.694*	0.696*	0.727*	0.734*
Gyirong	0.670*	0.792*	-0.192*	-0.341*	0.568*	0.403*	0.271*	-0.313*	0.571*	0.610*	0.327*	0.470*
QOMOS	0.731*	0.138	-0.244*	-0.086	0.533*	0.672*	0.086	-0.230*	0.920*	0.560*	0.488*	0.622*
Nyima	0.690*	-0.112*	0.058	0.088	0.564*	0.734*	0.161*	-0.168*	0.654*	0.399*	0.448*	0.477*
Coqen	0.518*	0.591*	-0.167	0.124	0.316*	0.423*	-0.007	-0.437*	0.542*	0.168	0.411*	0.439*
MAWORS	0.572*	0.362*	-0.550*	0.363	0.072	0.371*	-0.039	-0.094	0.715*	-0.013	0.279*	0.595*
NADORS	0.610*	0.228*	0.294*	0.119*	0.340*	0.590*	0.769*	0.168*	0.729*	0.721*	0.843*	0.809*
Burang	0.706*	0.060	0.364*	0.121*	0.681*	0.840*	0.012	0.099	0.486*	0.455*	0.093	0.284*
Mangai	0.804*	0.545*	0.663*	0.501*	0.664*	0.320*	-0.520*	0.043	-0.045	-0.255*	-0.398*	-0.112